

Hubble Space Telescope and Ground-Based Observations of Type Ia Supernovae at Redshift 0.5: Cosmological Implications^{1,2}

Alejandro Clocchiatti,³ Brian P. Schmidt,⁴ Alexei V. Filippenko,⁵ Peter Challis,⁶ Alison L. Coil,⁵ R. Covarrubias,⁷ Alan Diercks,⁷ Peter Garnavich,⁸ Lisa Germany,⁴ Ron Gilliland,⁹ Craig Hogan,⁷ Saurabh Jha,^{6,5} Robert P. Kirshner,⁶ Bruno Leibundgut,¹⁰ Doug Leonard,^{5,11} Weidong Li,⁵ Thomas Matheson,^{6,12} Mark M. Phillips,¹³ José Luis Prieto,^{14,15} David Reiss,⁷ Adam G. Riess,⁹ Robert Schommer,^{14,16} R. Chris Smith,¹⁴ Alicia Soderberg,^{5,11} Jason Spyromilio,¹⁰ Christopher Stubbs,¹⁷ Nicholas B. Suntzeff,¹⁴ John L. Tonry,¹⁸ and Patrick Woudt^{10,19}

Accepted for publication in Astrophysical Journal

¹Based in part on observations with the NASA/ESA *Hubble Space Telescope*, obtained at the Space Telescope Science Institute, which is operated by the Association of Universities for Research in Astronomy (AURA), Inc., under NASA contract NAS 5-26555. This research is primarily associated with proposal GO-7505.

²Based in part on observations taken at the Cerro Tololo Inter-American Observatory. Some of the data presented herein were obtained at the W. M. Keck Observatory, which is operated as a scientific partnership among the California Institute of Technology, the University of California, and the National Aeronautics and Space Administration. The Observatory was made possible by the generous financial support of the W. M. Keck Foundation. Based in part on observations with the University of Hawaii 2.2-m telescope at Mauna Kea Observatory, Institute for Astronomy, University of Hawaii. Based in part on observations obtained at the European Southern Observatory, Paranal and La Silla, Chile, under programs ESO 64.O-0391 and ESO 64.O-0404. Based in part on observations taken at the WIYN Observatory, a joint facility of the University of Wisconsin (Madison), Indiana University, Yale University, and the National Optical Astronomy Observatories.

³Pontificia Universidad Católica de Chile, Departamento de Astronomía y Astrofísica, Casilla 306, Santiago 22, Chile; aclocchi@astro.puc.cl.

⁴The Research School of Astronomy and Astrophysics, The Australian National University, Mount Stromlo and Siding Spring Observatories, via Cotter Rd, Weston Creek PO 2611, Australia; brian@mso.anu.edu.au.

⁵Department of Astronomy, 601 Campbell Hall, University of California, Berkeley, CA 94720-3411; alex@astro.berkeley.edu, acoil@astro.berkeley.edu, weidong@astro.berkeley.edu, sjha@astro.berkeley.edu.

⁶Harvard-Smithsonian Center for Astrophysics, 60 Garden Street, Cambridge, MA 02138; kirshner@cfa.harvard.edu, pchallis@cfa.harvard.edu.

⁷University of Washington, Department of Astronomy, Box 351580, Seattle, WA 98195-1580; hogan@astro.washington.edu.

⁸University of Notre Dame, Department of Physics, 225 Niewland Science Hall, Notre Dame, IN 46556-5670; pgarnavi@nd.edu.

⁹Space Telescope Science Institute, 3700 San Martin Drive, Baltimore, MD 21218; rgillila@stsci.edu, ariess@stsci.edu.

¹⁰European Southern Observatory, Karl-Schwarzschild-Strasse 2, Garching, D-85748, Germany; bleibund@eso.org, jsipyromi@eso.org.

¹¹Department of Astronomy, MS 105-24, California Institute of Technology, Pasadena, CA 91125; leonard@astro.caltech.edu.

¹²National Optical Astronomy Observatory, 950 N. Cherry Ave., Tucson, AZ 85719; matheson@noao.edu.

¹³Las Campanas Observatory, Casilla 601, La Serena, Chile; mmp@lco.cl.

¹⁴Cerro Tololo Inter-American Observatory, Casilla 603, La Serena, Chile; csmith@ctio.noao.edu, nsuntzeff@noao.edu.

¹⁵Ohio State University, Department of Astronomy, 4055 McPherson Laboratory, 140 W. 18th Ave.,

ABSTRACT

We present observations of the Type Ia supernovae (SNe) 1999M, 1999N, 1999Q, 1999S, and 1999U, at redshift $z \approx 0.5$. They were discovered in early 1999 with the 4.0 m Blanco telescope at Cerro Tololo Inter-American Observatory by the High- z Supernova Search Team (HZT) and subsequently followed with many ground-based telescopes. SNe 1999Q and 1999U were also observed with the *Hubble Space Telescope*. We computed luminosity distances to the new SNe using two methods, and added them to the high- z Hubble diagram that the HZT has been constructing since 1995.

The new distance moduli confirm the results of previous work. At $z \approx 0.5$, luminosity distances are larger than those expected for an empty universe, implying that a “Cosmological Constant,” or another form of “dark energy,” has been increasing the expansion rate of the Universe during the last few billion years.

Combining these new HZT SNe Ia with our previous results and assuming a Λ CDM cosmology, we estimate the cosmological parameters that best fit our measurements. For a sample of 75 low-redshift and 47 high-redshift SNe Ia with MLCS2k2 (Jha et al. 2005) luminosity calibration we obtain $\Omega_M = 0.79^{+0.15}_{-0.18}$ and $\Omega_\Lambda = 1.57^{+0.24}_{-0.32}$ (1σ uncertainties) if no constraints are imposed, or $\Omega_M = 0.29^{+0.06}_{-0.05}$ if $\Omega_M + \Omega_\Lambda = 1$ is assumed. For a different sample of 58 low-redshift and 48 high-redshift SNe Ia with luminosity calibrations done using the PRES method (a generalization of the Δm_{15} method), the results are $\Omega_M = 0.43^{+0.17}_{-0.19}$ and $\Omega_\Lambda = 1.18^{+0.27}_{-0.28}$ (1σ uncertainties) if no constraints are imposed, or $\Omega_M = 0.18^{+0.05}_{-0.04}$ if $\Omega_M + \Omega_\Lambda = 1$ is assumed.

Subject headings: cosmology: observations — distance scale — galaxies: distances and redshifts — supernovae: general

Columbus, Ohio 43210; prieto@astronomy.ohio-state.edu.

¹⁶Deceased 12 December 2001.

¹⁷Department of Physics and Department of Astronomy, 17 Oxford Street, Harvard University, Cambridge MA 02138; cstubbs@fas.harvard.edu.

¹⁸Institute for Astronomy, University of Hawaii, 2680 Woodlawn Drive, Honolulu, HI 96822; jt@ifa.hawaii.edu.

1. Introduction

1.1. Distances, Acceleration, and Deceleration

Studies of the distance versus redshift (z) relation of high-redshift Type Ia supernovae (SNe Ia) have produced persuasive evidence that we live in a Universe whose expansion rate is currently accelerating. This remarkable conclusion is the result of developments in empirical calibration strategies, instrumentation, and software, which converged to make SNe Ia very effective tools for estimating luminosity distances of very distant galaxies.

The relevant work can be traced back to the early 1990s, when the light-curve shape versus luminosity relation for SNe Ia was first clearly recognized (Phillips 1993). This breakthrough prompted the building of homogeneous samples of SNe Ia distant enough to be in the Hubble flow. SNe Ia were searched for, discovered, carefully observed, and used as benchmarks for calibrating empirical relationships between light-curve shape and luminosity (Hamuy et al. 1995, 1996a,b; Riess et al. 1995; 1996, 1998a; Perlmutter et al. 1997, 1999; Phillips et al. 1999).

In addition to these analytical tools, the measurement of precise luminosity distances to samples of high- z SNe Ia required large-format CCDs on 4.0-m class telescopes, sophisticated software for comparing images taken at different epochs, and efficient human organization to carry out the job. The first handful of distant SNe Ia already challenged the theoretically preferred cosmological model of the time: a zero-curvature universe closed by the mass density, $\Omega_M = 1$ (Garnavich et al. 1998a; Perlmutter et al. 1998).

When the distant SN Ia samples became large enough to reduce the statistical noise of the combined distance moduli to a few hundredths of a magnitude, evidence that the Universe is currently accelerating became clear: at $z \approx 0.5$, the distances are larger than expected for a universe with any degree of deceleration (Riess et al. 1998a; Perlmutter et al. 1999). This result was reached using two different samples of distant SNe Ia by two different groups of astronomers and physicists, the High- z SN Search Team (HZT, led by B. P. Schmidt; Schmidt et al. 1998), and the Supernova Cosmology Project (SCP, led by S. Perlmutter; Perlmutter et al. 1997). This helped lend credence to the controversial result. The two groups used the same observables (luminosity distances and redshifts of high- z SNe Ia), but the fact that they had different discovery and analysis tools provided some resilience against systematic effects.

More recent observations confirm and extend the 1998–1999 findings. Tonry et al. (2003), Knop et al. (2003), and Barris et al. (2004) use SN Ia samples, observed with the *Hubble Space Telescope (HST)* and ground-based telescopes, to demonstrate that the results

of Riess et al. (1998a) and Perlmutter et al. (1999) were not a statistical fluke. Distances of SNe Ia at $z \approx 0.5$ are confirmed to be larger than those predicted for an empty universe. In addition, Tonry et al. (2003) and Barris et al. (2004) find that the result is likely due to cosmology, not to an unrecognized systematic effect: at $z \gtrsim 0.7$ the trend appears to be reversed, with luminosity distances growing with redshift at a rate *slower* than that predicted by an empty universe. This effect is more convincingly shown by Riess et al. (2001) and Riess et al. (2004) with *HST* observations of SNe Ia at $z > 1$, strongly suggesting that the Universe was decelerating at early times.

The widespread interpretation of the combined high- z SN Ia observations has been that the Universe has a “Cosmological Constant,” or some other form of “dark energy” accelerating its present rate of expansion. Reviews with more detail on this remarkable paradigm shift are given by Riess (2000a), Leibundgut (2001), Carroll (2001), Perlmutter & Schmidt (2003), and Filippenko (2001, 2004, 2005).

The Hubble diagram of distant SNe Ia is not the only experiment suggesting the presence of dark energy and an accelerating universe. The best-known method is the combination of observations of the power spectrum of fluctuations in the cosmic microwave background radiation (CMBR) with independent measurements of the mass-density parameter from galaxy clusters. The former favors a Universe with $\Omega_{total} = 1.0 \pm 0.02$ (de Bernardis et al. 2002; Spergel et al. 2003), while the latter indicates that $\Omega_M \approx 0.3$ (Peacock 2001), or perhaps even lower ($\Omega_M \approx 0.19$, Bahcall et al. 2003). These results indicate that a significant contribution from dark energy is necessary to produce the nearly flat geometry of the Universe, although they do not provide direct evidence for *acceleration*.

Very recently, two other experiments produced results that support the presence of dark energy. First, studies of the Integrated Sachs-Wolfe (ISW) effect based on the cross-correlation between the Sloan Digital Sky Survey sample of galaxies and the temperature of the CMBR measured by the Wilkinson Microwave Anisotropy Probe (Afshordi, Loh, & Strauss 2004; Boughn & Crittenden 2004; Fosalba et al. 2003; Nolte et al. 2004; Scranton et al. 2005). The cross-correlation is achromatic and shows more clearly in the subsamples of galaxies at larger mean redshifts ($z \approx 0.43, 0.49$, and 0.55) for which the null hypothesis (i.e., no dark energy) is excluded at $>90\%$ confidence. Although this test provides physical evidence for the existence of dark energy, it cannot give details on its nature because the ISW effect is essentially independent of the dark-energy properties.

Second, Allen et al. (2004) use Chandra observations of the largest, apparently relaxed, galaxy clusters to set joint constraints on the dark energy and mass density parameters. They use the dependence of the derived baryonic mass fraction on the angular diameter distances to the clusters, plus the *assumption* that this baryonic mass fraction should be

constant with redshift for the largest clusters, to set a test for the reference cosmology: the baryonic mass fraction will appear to be constant only if the angular diameter distances are computed with the correct cosmological model. They obtain a clear detection of dark energy (greater than 3σ), although one may question the assumptions that the clusters are relaxed and have a constant baryonic mass fraction.

1.2. The Continuing Test

The convergence of independent observations to a unified “concordance” vision of the Universe — with low mass ($\Omega_M \approx 0.3$), a large component of dark energy ($\Omega_\Lambda \approx 0.7$, where we use Λ generically for dark energy), and zero curvature (preserving the initial condition favored by inflation) — has a very strong appeal to cosmologists and astrophysicists, and the results are now taken as nearly certain. Nevertheless, the HZT has been committed to continue testing the result by reducing statistical uncertainties and constraining systematic effects with more certainty.

Probing alternative interpretations of the apparently dimmer than expected SNe Ia remains important now, but it was particularly pressing in 1998, when the observational campaign reported in this paper was conceived. Alternatives seriously viewed at the time were as follows. (a) Some of the high- z SNe had been misclassified due to low signal-to-noise ratios (S/N) in spectra and light curves; they were actually subluminous SNe Ia, or even the fainter SNe Ib/Ic, biasing the average derived distances toward larger values. (b) Some of the high- z SNe Ia had been made dimmer by an anomalous “grey” extinction, caused by dust in the form of carbonated needles instead of the typical grains of carbon, iron, and silicates. (c) The objects were drawn from a SN Ia sample statistically different from the nearby population, making a direct comparison unwarranted. (d) SNe Ia were not standard candles in a cosmological sense, but subject to evolutionary effects that made them intrinsically dimmer with lookback time. These issues were pondered by Schmidt et al. (1998), Riess et al. (1998a), and Perlmutter et al. (1999). Although there were, at the time, strong reasons to suggest that none of them implied an effect large enough to nullify the apparent acceleration of the Universe, they were considered important matters of concern that needed to be experimentally addressed.

Each one of the previous alternative explanations could be tested through specific observational strategies. Item (a) required better spectroscopy and photometry of the high- z SN candidates, preferably over a wavelength range extending to rest-frame infrared. For example, one of the clearest differences between normal and subluminous SNe Ia (or SNe Ib/Ic) is the infrared light curve which respectively shows, or does not show, a secondary maximum.

Optical spectra having larger S/N, and extending as far to the red as possible, were also a high priority. Regarding (b), multicolor photometry extending to infrared wavelengths was desired. No “grey” dust produces a completely grey extinction (Aguirre 1999a,b). Although the $B - V$ color excess of dust needles is smaller than observational uncertainties, the color excess over wider wavelength intervals is larger and may be tested. Therefore, one of the first priorities after the work of Riess et al. (1998a) was to obtain rest-frame I_c photometry of high- z SNe Ia, through observations in the infrared J band ($1.2 \mu\text{m}$).

Item (c) above is difficult to resolve, but probably has a limited impact because high- z and low- z SNe Ia are not statistically compared as populations but as individuals, and each one of them is individually calibrated in luminosity using its own light-curve shape. After correcting for light-curve shape, the intrinsic dispersion in luminosity of SNe Ia is very small (Riess et al. 1995; Hamuy et al. 1996a; Phillips et al. 1999; Jha 2000; Germany 2001), implying that any residual Malmquist bias will be minimal (see the discussion in Schmidt et al. 1998). Contaminants of the sample like SNe Ic, which have a much broader distribution in luminosity, might introduce a luminosity bias. The impact of putative differences in population, both of SNe Ia and contaminants, is reduced simply by increasing the S/N of the observations, thereby providing better discrimination between normal and peculiar SNe and improving the brightness calibration of each individual event. So, a second obvious priority that we set for the campaigns following 1998 was to increase the S/N as much as possible, if necessary restricting the number of objects to monitor, in a “quality over quantity” approach.

Finally, evolutionary effects in the light sources, item (d) above, traditionally pose an insurmountable problem for any Hubble diagram at high redshift, since detailed knowledge of the source evolution with lookback time is required. In this particular case, however, astronomers have a simpler solution. Current estimates of Ω_Λ imply that its dynamic effect started to dominate over that of Ω_M a few billion years ago, with the redshift of the transition being $z_T \approx 0.5$ (Riess et al. 2004). At redshift larger than z_T , luminosity distances in a low mass, decelerating (at that time) universe should grow more *slowly* with increasing redshift than in an empty universe. By observing SNe beyond $z_T \approx 0.5$, the issue of evolutionary (and other systematic) effects can be experimentally tested.

The observational campaigns of the HZT from 1999 onwards were designed with these concerns and strategies in mind. The first HZT campaign of the year 1999, the one reported here, was designed to address items (a), (b), and (c) above. Its goal was to obtain superior-quality light curves and spectra of a few SNe at a redshift of ~ 0.5 to provide a point in the Hubble diagram with high statistical significance at this critical redshift.

The SN search was programmed at Cerro Tololo Inter-American Observatory (CTIO),

and spectroscopic confirmation was done at the Keck-1 10 m telescope. Follow-up observations were conducted at several ground-based telescopes and with the *Hubble Space Telescope* (*HST*). Telescopes that delivered images useful for the SN light curves presented here were the Keck-1 and Keck-2 telescopes (Keck Observatory), VLT-1 (ESO-Paranal Observatory), the 3.5 m telescope at Apache Point Observatory, the 3.6 m telescope at ESO-La Silla Observatory, the 2.2 m telescope of the University of Hawaii (Mauna Kea Observatory), the 4.0 m and 1.5 m telescopes at CTIO, and *HST*.

As a side project of this campaign, we observed SN 1999Q in the J band. We transformed the observed J data into rest-frame I_c , studying the infrared properties of this SN and searching for the color signature of relatively “grey” reddening by dust. These results were published by Riess et al. (2000b). Briefly, we found that SN 1999Q was a normal SN Ia, and there was no evidence for non-standard extinction.

In § 2 we describe our search campaign, the follow-up spectroscopic and photometric observations, and the calibration of the local sequences of standard stars. We present and describe the observed-frame SN photometry in § 3. Section 4 describes the transformation of the observed-frame photometry into the rest frame of each SN, together with the methods of light-curve fitting, K-correction, and luminosity calibration. We analyze and discuss the results in § 5, presenting updated high- z Hubble diagrams and using them to fit cosmological parameters.

2. Observations

2.1. Search, Discovery, and Confirmation

Three nights with the 4.0 m Blanco telescope at CTIO had been allocated for this search: 1999 January 13, 14, and 17 (UT dates are used throughout this paper). The telescope was equipped with the “Big Throughput Camera” (BTC; Wittman et al. 1998), a prime focus mosaic imager with four SITe 2048×2048 pixel CCDs, a field of view of 0.24 square degrees, and a pixel scale of $0.43'' \text{ pix}^{-1}$.

No time for first-epoch observations could be scheduled during the previous lunation. Instead, the image comparison to detect transient sources was done with templates obtained during the campaigns of 1998 (Suntzeff et al. 2006, in preparation), approximately a year earlier. This made the search vulnerable to objects such as quasars, which vary on a time scale longer than SNe Ia near maximum brightness. The search was also prone to the discovery of SNe many days after maximum, when their utility as distance estimators is very limited. Our strategy to refine the sample before investing spectroscopic time was to search for SN

candidates as rapidly as possible, repeat images of the candidate fields during the nights between discovery and spectroscopy, and apply photometric cuts based on preliminary light-curve evolution and colors of the transient sources. Additional criteria included the presence of a suspected host galaxy, and the projected distance of the transient source from the galaxy nucleus.

The pipeline used for image reduction and analysis is described by Schmidt et al. (1998). Briefly, it starts at the mountaintop, where the BTC images are trimmed, bias-corrected, flat-fielded, and defringed (if necessary) with standard IRAF¹ tasks. Images are then transferred to a network of workstations at the CTIO headquarters in La Serena, where they are aligned, matched in point-spread function (PSF) shape and intensity with the template frames, and subtracted. The residual images are searched using a PSF detection algorithm, and a list of candidate transient sources is generated for human experts to inspect by eye.

The search and photometric confirmation of candidates at CTIO was very successful, providing 37 transient sources deemed sufficiently good for subsequent spectroscopy. Of these, 14 candidates were given first priority and another 14, second. Priorities were assigned according to apparent brightness, change of brightness between different epochs (when available), color, presence of a putative host galaxy, and position of the candidate with respect to the galaxy nucleus. The 9 remaining events were considered true transient stellar-like sources. However, they had a combination of brightness, color, and absence of a host galaxy that made them unlikely to be SNe useful for our science goals, and were thus dropped from further consideration.

2.2. Keck-1 Spectroscopy, SN Classification, and Selection

Spectroscopy of the selected SN candidates was done with the Low Resolution Imaging Spectrometer (LRIS; Oke et al. 1995) at the Cassegrain focus of the Keck-1 telescope. Five nights (1999 January 17–21) had been allocated to our program. Skies were clear most of the time, with only three hours of the last night lost to fog. The atmospheric seeing was mediocre, however, with a median value close to 2'' and typical variations between 1.2'' and 2.5''. Spectra were obtained in long-slit mode, with a slit width of 1.0'' or 1.5'' depending on the seeing. The spectrograph was rotated to include in the same slit the SN candidate and a nearby star.

¹The Image Reduction and Analysis Facility is developed and maintained by NOAO, under contract with the National Science Foundation.

Reductions of the two-dimensional (2D) spectra were done following the typical procedures (e.g., Matheson et al. 2005) and using IRAF tasks. The bias level was removed using the overscan regions, and the 2D spectra were flat-fielded with dome flats. The location of the nearby star on the detector as a function of position along the dispersion was used to define a trace, which was then shifted and centered on the SN candidate to improve the quality of the extraction. Care was taken to model the light of the background sky, including the host galaxy when present, to minimize contamination of the SN candidate spectrum. Since the typical angular size of the surface brightness variations in these fairly high-redshift galaxies is similar to both the slit width and the seeing, it is impossible to completely remove the background and some contamination remains.

Despite the mediocre seeing, the Keck-1 observers managed to take spectra of the 28 candidates of first and second priority. One half of them were recognized as SNe: nine were classified as SNe Ia, four as SNe II, and one as a SN Ic. Five additional candidates were quasars. Nine of the spectra could not be assigned to any kind of known object. In three cases, this happened even though the spectra had decent S/N.

Five of the nine SNe Ia were selected for follow-up observations, including *HST* imaging for two of them. Selection of the SNe was based on a combination of their redshift, their initially assigned priority (which essentially grades their quality with photometric criteria), and their spectroscopic age. SNe Ia at $z \approx 0.5$, with normal colors, and not very close to the nuclei of bright host galaxies were given the highest priority for follow-up observations. Brief information on all the spectroscopically confirmed candidates was provided by Garnavich et al. (1999). Figures 1 to 5 give finder charts of the five SNe Ia analyzed in this paper. Note that the pixelization of the ground-based and *HST* images differs, for approximately the same field of view.

Table 1 summarizes additional information on the chosen SNe Ia. We give their position in the sky, the foreground Galactic extinction from Schlegel et al. (1998), and the total number of images accumulated from various telescopes, including the very late-time images obtained when the SNe had faded away. The table includes all the images that were collected in this study’s database, even though some of them were subsequently combined into one, and some others were discarded due to low S/N or very poor seeing. The photometric follow-up campaign resulted in more than 300 images taken with nine different telescopes. The total number of images for each SN is a good indication of its assigned priority.

The concentration of spectroscopic time on just a few candidates resulted in high S/N. It ranges from ~ 15 for SN 1999Q, our highest-priority object, down to ~ 6 for SN 1999M and SN 1999N. The latter two had been given low priority because of the bright background of their host galaxies. Figures 6 to 10 show the final Keck-1 spectra. For comparison, we also

include spectra of nearby SNe Ia at early phases combined with the spectrum of a galaxy from the catalog of Kennicutt (1992).

Table 2 gives additional details of the spectroscopy: the method used to obtain the redshift of each SN, the approximate phase of the spectra obtained from the spectral-feature age method (see Riess et al. 1998b), and the phase implied by two different light-curve fits to be described in § 4. The redshifts given in Table 2 are slightly different from those initially reported after a quick analysis during the search (Garnavich et al. 1999), and supersede them.

It is clear from the figures that all the objects selected are SNe Ia without obvious spectroscopic peculiarities, and that they were detected at early phases. Near maximum light, typical SNe Ia show a strong Si II absorption line at rest-frame wavelength ~ 615 nm (the strongest Si II line in the optical/near-IR range). Although the redshift of the objects places this line out of the CCD sensitivity window, all spectra display the second-strongest silicon line in this range, Si II $\lambda 4130$, which appears close to rest-frame 400 nm. This confirms that our SNe are not Type Ib/Ic events, for which this secondary Si II line is essentially absent (Clocchiatti et al. 2000; Coil et al. 2000).

Figures 6 to 10, in addition, detail the basic elements used to match the observed spectra. These elements are the spectrum of a nearby SN Ia at early phases and the spectrum of a galaxy from the catalog of Kennicutt (1992), but we found it necessary to add an additional slope to make its continuum redder. All of the observed spectra appear too red to match the model of a SN contaminated by a galaxy. It is possible to make the combined SN-plus-galaxy spectra redder by resorting to galaxies with extremely red spectra, or by increasing the fraction of light from the galaxy in the combination. There is, however, a limit to the amount of light from a galaxy that the combination can tolerate since the contrast between maxima and minima of the SN features is changed by galaxy contamination. Also, there are cases where the continuum of a red galaxy improves the contrast between the red and blue spectral regions (i.e. the color of the model), but does not improve the overall fit. A straight line, as shown in the figures, simply does a better job.

The case of SN 1999Q is especially illustrative. All the information obtained on this event, including the very deep image obtained by combining the *HST* exposures, indicates that its host galaxy has very low luminosity. The spectrum in Figure 8 confirms this. The contribution from a galaxy spectrum is very small, at most around 20%, while the need for a smooth trend to make the spectrum redder than that of SN 1992A is apparent.

There is a somewhat independent way of testing this conclusion. For two of the objects (SN 1999S and 1999U) it is possible to compute a synthetic color from the spectrum and

compare it with the observed photometry. For both SNe the synthetic $R_c - I_c$ result is ~ 0.5 mag, about half a magnitude redder than the observed $R_c - I_c$ color close to maximum light, the time at which the spectra were taken (cf. Tables 12 and 13). The spectra used to compute the synthetic colors, however, include the unknown contribution from the host galaxy, which is likely to be redder than a SN Ia near maximum light. Red galaxies, like the one used to model the observed spectra in figures 6 to 10, at $z \approx 0.5$ will have observed $R_c - I_c \approx 1$ mag. It is possible to combine light from a red galaxy and a blue SN to modify the observed SN color ($R_c - I_c \approx 0.0$ mag) and make it similar to the synthetic color ($R_c - I_c \approx 0.5$ mag), but unrealistic parameters are required to do so. One would need, for example, more than 50% of the light in the slit to be from the galaxy, *and* that the spectrum of the galaxy be 50% brighter than that of the SN in the observed I_c band (rest-frame V). A bluer galaxy will accomplish the same thing with more light contamination, or an even redder galaxy will suffice with a smaller contamination. It is unrealistic to think that these kinds of extreme combinations are needed to fit both cases, especially since both spectra exhibit [O II] $\lambda 3727$ emission (a line not associated with particularly red galaxies).

We have convinced ourselves that the spurious slopes are not intrinsic to the spectra, but unfortunately we cannot offer a reasonable explanation. Since it appears to be independent of the amount of galaxy background and color, which differ among the SN spectra, it is probably an instrumental, or reduction, effect. Its existence introduces a free parameter in the spectroscopic match, and our attempt to keep this slope to a minimum biases the spectra of the background galaxy to the red: spectra of red galaxies match our observations better than spectra of bluer galaxies. All the spectra shown were fitted using as a background model the spectrum of NGC 3379, one of the reddest galaxies in the sample of Kennicutt (1992).

Phases (i.e., SN ages) obtained from background-contaminated SN Ia spectra are more uncertain than those obtained from the spectra of well-isolated SNe Ia (Riess et al. 1997). When the background-to-SN light ratio increases, the contrast between maxima and minima of SN features diminishes, mimicking a younger SN. Furthermore, some of the observed spectra shown here are the combination of exposures taken over the span of up to five nights (~ 2.7 rest-frame days). At early phases, the spectrum of a SN Ia can vary significantly on timescales as short as 1–2 days. Hence, some of our spectra should not be considered as being representative of a single phase, but rather as a time average, and time averaging during the photospheric phase changes the contrast of SN spectral features. Both the background contamination and the time averaging increase the uncertainty of the spectroscopic phase estimate. The spectrum comparisons shown in figures 6 to 10 are thus somewhat qualitative. They are approximately correct, but given the large number of essentially free and degenerate parameters involved in the matching problem, we do not claim that they

necessarily correspond to the best fit of an objective minimization scheme.

2.3. Calibration of Photometry

2.3.1. Ground-Based Images

We measured the brightnesses of the SNe in ground-based images by computing relative magnitudes with respect to a local standard sequence. The calibration of these sequences was done entirely with the CTIO 1.5 m telescope. Seven nights were granted for this in mid-February 1999. The telescope was equipped with the Cassegrain focus CCD camera. Two different focal ratios were used, $f/18$ and $f/13$, giving a scale of $0.39''$ pixel $^{-1}$ and $0.28''$ pixel $^{-1}$, respectively.

During the calibration nights, repeated images of the SN fields together with images of Landolt (1992) standard-star fields were obtained. The 1.5 m telescope was equipped with the typical passbands used by the HZT. These included the R_c and I_c bands of the Kron/Cousins system (Kron & Smith 1951; Cousins 1976), and the custom bands $B45$ and $V45$ — the special filters designed by the HZT that correspond to the Johnson (1955) B and V bands (respectively) at $z = 0.45$ (Schmidt et al. 1998). During four of the seven nights, images in both filter sets were taken. Each photometric system was treated as a separate set and their images considered independently. The calibration campaign resulted in ~ 640 additional images to analyze.

All the images from the calibration nights were reduced in the standard way within the IRAF environment. The electronic pedestal was subtracted using the overscan area of the CCD, and the bias images were checked for a 2-dimensional residual pattern that the overscan correction could not remove. Although this residual was consistent with no signal, it was in each case subtracted anyway because its noise level was also minimal. Dome flats were used to normalize the pixel-to-pixel sensitivity variations. Image airmasses were corrected to their effective value using the task SETAIRMAS of the IRAF package DAOPHOT.

For the images containing the standard-star fields, we recognized the fields by eye, checked the profiles of the standard stars for signs of cosmic rays, CCD defects, or saturation, and did aperture photometry of those that did not show problems. The adopted apertures ($7''$ – $12''$) varied with the typical seeing of the images of each set. Photometry was done using DAOPHOT tasks in IRAF.

Once the photometry of the standard stars was done, we fitted the parameters for the

filter set using equations of the form

$$m_R = R + Z_R + \kappa_R X_R + C_{RI}^1(R - I) + C_{RI}^2 X_R(R - I), \quad (1)$$

where m_R is the observed magnitude in the R band, R is the magnitude of the star in the standard system, Z_R is the R -band zero point, κ_R is the extinction coefficient in the R band, X_R is the airmass for the R -band observation, C_{RI}^1 is the color term in $R - I$, and C_{RI}^2 is the cross term in $R - I$. This was done for each of the nights, and for each of the photometric systems observed. Ultimately, the seven calibration nights gave rise to eleven different photometric calibrations.

Five of the seven nights provided results that were consistent within the uncertainties, as well as with the typical values at the CTIO 1.5 m telescope, and were considered photometric. For the other two nights, either the extinction coefficients or the color terms (or both) were significantly different, prompting us to eliminate them from further consideration. For all the photometric nights, and the two photometric systems, the cross terms (C_{RI}^2 fitted in equation 1) were consistent with zero and were set to zero for the definitive fit.

The images of the SN fields were searched for stellar objects using SExtractor (Bertin 1996), and the list of stars provided by the program was refined by eye. We selected fairly extensive sets of local standards, typically between ~ 20 and ~ 40 , because of the need to calibrate images taken with very different parameters (e.g., CCD fields of view) at different telescopes. The brightnesses of local standards were measured with PSF-fitting photometry using the IRAF/DAOPHOT tasks and procedures. The PSF photometry of the local standards was usually calibrated with small apertures, because some of these standards were rather faint or had relatively close apparent companions. The transformation of this photometry to the larger apertures of the photometric system standards was done with aperture corrections defined by bright, well-isolated local standards. With the instrumental magnitudes in hand, we inverted the systems of equations like Eq. (1), and obtained calibrated magnitudes for the sequences of local standards.

The extensive sets of local standards proved to be very useful. By calibrating local standards with a wide color range, it is possible to check whether color terms are important for the different combinations of telescopes and instruments used. Moreover, if necessary, the color terms can be estimated from the SN frames, without a set of all-sky photometric standards observed with the same combination of telescopes and instruments. Finally, by having local standards with a wide range of brightnesses, it is possible to calibrate images with very different depths, like those obtained in this campaign where 1.5 m to 10 m telescopes were used.

2.3.2. *HST* Images

We calibrated the SN brightnesses in the *HST* images independent of any local sequence of standard stars. The *HST* images were reduced using the “On-The-Fly Reprocessing” image reduction pipeline, provided by the Space Telescope Scientific Institute (STScI). Images had been taken in pairs to eliminate cosmic rays with the task CRREJ of the IRAF package STSDAS, which uses the two observed images combined with knowledge of the noise characteristics of the *HST* WFPC2 to remove cosmic rays. PSF-fitting photometry of the stars in the *HST* frames was done using HSTPhot (Dolphin 2000), which is calibrated with the zero points of Holtzman et al. (1995), by normalizing the PSF magnitude to aperture photometry with $0.5''$ radius.

For the local standard sequences of the SNe that were observed both from ground-based telescopes and *HST*, therefore, we had two independent measurements to check the calibration. We compared the photometry of all stars in common between the *HST* WFPC2 and ground-based fields, finding the results to be consistent with the relations provided by Holtzman et al. (1995) for ground-based and *HST* stellar photometry as a function of color index. Suntzeff et al. (2006, in preparation) provide more detail of this analysis, which increases the reliability of our photometric calibration. Tables 3 to 7 present R and $R - I$ for the local sequences of standards, and Figures 11 to 15 give their finding charts.

3. SN Photometry in the Observed Frame

3.1. Images With and Without the Supernovae

All the images of SN fields were reduced following the standard techniques, with slightly different procedures depending on the telescope used. Observations of a given field were typically split into at least 3 images with small shifts between them, to facilitate rejection of cosmic rays and CCD defects.

We had a special case where the number of images to combine was unusually large. Two runs with the CTIO 1.5 m telescope having nights with a fairly bright moon were far from our other scheduled nights to do SN photometry, and were thus important for the temporal coverage of the objects. We obtained up to 30 images of each SN field, with a total exposure time of > 50 min per field, to greatly decrease the sky noise (an approach resembling that used for infrared photometry).

Most of our ground-based observations in the I_c passband showed substantial interference fringes. In these cases, the observers used multiple dithered images in different parts

of the sky to prepare a “fringe frame.” This fringe frame was obtained by combining all the I_c frames having the same exposure time on a given night with a median rejection algorithm. After subtraction of the fringe frame, the I_c images displayed a significantly flatter background.

Note that the noise pattern in the background is altered when the fringe frame is subtracted. In regions of the image where the fringes had been determined by combining essentially empty sky, the root-mean-square (RMS) in the background is unchanged. In regions of the image where the fringe pattern emerged after combining pixels with high signal (i.e., where bright stars or extended objects were present), the RMS of the background usually increased. We found increases of up to $\sim 15\%$ in the background RMS in a few regions of some images. These regions, however, were always far from the SNe, since we had chosen to follow SNe that were far from bright stars or bright extended objects.

The processed SN images were carefully analyzed by eye, with special attention given to the regions of the SNe and host galaxies. A few images were discarded because CCD or processing defects were visible near the SN position. In general, this did not significantly decrease the S/N; we typically had many images taken at similar epochs with different telescopes.

In order to perform unbiased photometry, a good model of the brightness distribution underneath the SN, for each particular image, is necessary. We built these “templates” from images of the field taken either the previous season, or more than a year after SN discovery when the SN had faded well below the detection limit. It is imperative that the template image have high S/N, excellent seeing, and good PSF shape. Table 8 gives a list of template images obtained for each SN and photometric band. In some cases we had more than one of these templates, allowing us to study the effect that template matching and subtraction has on the final photometry.

Template images taken with ground-based telescopes were reduced and combined following the standard procedures. The templates obtained with *HST* required special treatment. Originally, one very late-time visit had been scheduled to take images of the field and host galaxy when the SN had faded away. This last visit consisted, for each SN field and filter, of two images with the same exposure parameters as had been used for the longest images taken when the SN was still bright. Hence, we expected the same S/N in the template image as in the best images containing SNe. One would actually prefer a template with significantly *higher* S/N than the SN images, but this was a reasonable compromise given the limited amount of time allocated to our program. Unexpectedly, however, the *HST* images taken in March 2000 were noisier than the images of early 1999. Subtraction of the templates would have produced a considerable reduction in the quality of our *HST* SN photometry.

Instead, we proceeded as follows. We registered and combined all the *HST* images for each field, and used this very high S/N image to determine a good center for the SN. We constructed the PSF for Chip 3 of each *HST* field (the chip containing the SN) using all the isolated stars available on that chip. We then fitted the PSF to the SN and subtracted it from the image, leaving the center fixed at the position computed in the combined image. Next we combined all the images with the SN subtracted, and checked very carefully (line by line, and column by column) the place where the SN had been. We found, in general, an increase of the noise at this position, but no systematic anomalies with respect to the pixels in regions not affected by the PSF subtraction. When bad pixels or cosmic rays remained near the position of the SN, they were excised by hand. After this, we combined all the images with the SN subtracted, together with those of March 2000, rejecting any remaining bad pixels and cosmic rays. This combined image was our final template to subtract from the *HST* SN images.

To produce an *HST* template for ground-based images, we convolved the *HST* template with a symmetric kernel wider than the *HST* PSF, to make the resolution of the images $\sim 0.55''$ (as explained below, this is required by the PSF-matching software to work). These images are called “version 2” in Table 8.

3.2. SN Photometry of *HST* Images

Although noisy enough to prevent their adoption as templates, the March 2000 *HST* images of SN 1999Q and 1999U proved useful to simplify the SN photometry of the *HST* images. We verified in the March 2000 images that no signal from the host galaxies was present within $0.5''$ of the SN position, thus allowing us to use the typical strategies for *HST* stellar photometry.

We conducted PSF-fitting photometry with the package HSTPhot (Dolphin 2000), using the mid-2003 version of the package, zero points, and charge-transfer efficiency (CTE) correction parameters. We applied HSTPhot to the images as they were provided by STScI, with the reduction pipeline updated as well to mid-2003 (Dolphin 2003).

As a check, we subtracted the *HST* template from the *HST* images and did aperture photometry of the SNe, applying the same zero points and CTE corrections as HSTPhot. We found, not surprisingly, that the results were consistent within the uncertainties.

Finally, the noisier March 2000 *HST* images were used to obtain upper flux limits to the host-galaxy contribution, by doing aperture photometry within a radius of $0.5''$, the same as for the SN photometry. We found the same upper limits for both SN 1999Q and SN 1999U:

$R = 26.19 \pm 0.50$ mag, and $I = 25.76 \pm 0.35$ mag.

The *HST* photometry is included in Tables 11 and 13. Comparing the brightnesses of the SNe in the latest images with the upper limits quoted above, we confirm that the SNe were at least approximately five times brighter than the background. In addition, we see that subtraction of the March 2000 images would have meant uncertainties of $\sim 10\%$ in R and $\sim 7\%$ in I , solely from the template noise. Not using template subtraction meant a modest improvement in the uncertainties, at the expense of doing PSF-fitting photometry on a background essentially that of the sky.

3.3. Image Matching, Subtraction, and SN Photometry in Ground-Based Data

For each SN passband set, one of the best images (SN well centered, good seeing) was selected as astrometric reference, and all the other images were registered to match it. The registration was done using IRAF tasks. A registration map was built with GEOMAP by using matched objects in image pairs, and then the transformation was applied using GEOTRAN. After registration, we compared the centers of the objects in both images and computed the RMS of the differences. Our goal was to obtain an RMS smaller than 0.2 pixels. For small fields of view, it was generally possible to meet this goal using simple linear transformations (rotations plus translations). For frames with a wide field of view, however, it was typically necessary to fit distortion terms.

With the images registered, we matched the PSF and intensity scale of the template to those of the SN images. For each image/template pair, we selected objects with good S/N and compared their brightness distributions to find the two-dimensional difference kernel that, when convolved with the image having the better seeing (usually the template), matches the PSF of the other. We performed these tasks using a custom version of ISIS (Alard & Lupton 1998). ISIS builds a set of subrasters of the images around selected objects (these are called “stamps”), and compares the image/template pairs of stamps to find the difference kernel. The version we used differs from the original in that it iterates the stamp-selection stage, checking the residuals of each stamp after matching is done, rejecting stamps that leave large residuals, and recomputing the kernel until convergence is obtained. With the images matched in PSF shape and intensity, it was possible to subtract the template from the SN image and obtain, as a result, the SN PSF over an essentially constant background.

We found that ISIS performs well in situations where the full-width at half maximum (FWHM) of the two compared PSFs is moderately different. It does not provide good

matches when they are too different, or when they are similar in FWHM but differ in other shape characteristics, such as asymmetries oriented along different axes. In particular, it was not possible to find a difference kernel to convert the *HST* PSF into a ground-based telescope PSF. To obtain a successful matching between ground-based and space-based PSFs, it was necessary to degrade the resolution of the *HST* images, increasing the FWHM to $\sim 0.55''$. We did this by convolving the *HST* templates with a Gaussian symmetric kernel having a FWHM of 2 WFPC2 pixels.

Photometry of each SN was done on the subtracted image, but the image with the SN before background subtraction was used to fit the PSF shape and intensity scale. For this, we followed the typical steps of PSF photometry, using the tasks of IRAF package DAOPHOT. A set of stars suitable to do photometry was selected by eye, centers for them were computed by fitting Gaussian kernels to the cores, and aperture photometry (without recentering) was done. A subset of these stars was used to compute the PSF of the frame in the DAOPHOT style, with a theoretical function fitted to the core and a numerical residual computed to match the wings. About 90% of the time, the best-fitting theoretical function was a combination of a Gaussian core with Lorentzian wings (called “penny” in IRAF tasks), and Moffat functions were the best fit in the remaining $\sim 10\%$ of the cases. With the PSF computed, we performed PSF photometry for all the selected stars in the image, and checked residuals to judge the quality of the PSF fitting. The process of PSF fitting and subtraction was repeated until sufficiently small residuals were obtained. In most cases, this required the use of a variable PSF, depending on the angular size of the image and the combinations of telescope/instrument used in the template/image pair. When computing the PSF, the star centers were left as a parameter to fit.

The PSF of the frame was then fitted to the residual image of the SN in background-subtracted frames. The position of the SN was fixed, however, to avoid shifting of the PSF toward locally “hot” pixels (i.e., pixels that happened to contain more signal due to statistical variations). Uncorrected, this effect would produce systematically higher flux estimates and flatter light curves on the SN tails, when S/N is low. The SN position was obtained by combining all the background-subtracted images that showed a residual PSF after subtraction of the template.

We then generated a set of 20 artificial stars with the same flux as the SN, positioned them in places having background similar to that of the SN, and repeated the procedure to recover their instrumental magnitudes via PSF photometry. This procedure allowed us to check the RMS in the SN photometry, and to see whether a systematic intensity shift existed for the PSF of each particular frame. With a couple of exceptions in the case of SN 1999M, the shifts found were smaller than the RMS.

With the instrumental magnitudes of stars around each SN, we could fit a zero point and color term, using equations similar to Eq. (1). When we had images of the SN in at least two passbands, we could invert the system and obtain the magnitude of the SN in both bandpasses. In the few cases when we had only one passband for the SN, we interpolated the other band from nearby epochs and used the interpolated value to compute the color-term correction. We used subsets of local standards with color similar to that of the SN to minimize the effect of the color terms and reduce the uncertainty.

4. SN Photometry in the Rest Frame

4.1. K-corrections and Light-Curve Fitting

The procedure described above provided us with SN magnitudes in our frame of reference, the observed frame. To obtain the rest-frame magnitudes, which we need to compare with the local sample of SNe Ia, it is necessary to apply a K-correction.

We computed the K-corrections and fitted the SN light curves simultaneously. We used two methods of light-curve fitting. Each one of them employs a slightly different approach to the K-corrections. In one case, cross-filter K-corrections as in Kim et al. (1996) and Schmidt et al. (1998) are computed. In the other, the method of Nugent et al. (2002) is closely followed.

As in Tonry et al. (2003), we write the apparent brightness of a SN observed in filter o , $m_o(t)$, having a $z = 0$ absolute magnitude light curve in filter r , $M_r(t')$, as

$$m_o(t) = M_r((1+z)t') + 25 + 5 \log \left(\frac{d_{lum}}{\text{Mpc}} \right) + K_{ro}((1+z)t'), \quad (2)$$

where K_{ro} is given by

$$K_{ro} = 2.5 \log \left[(1+z) \frac{\int F_\lambda(\lambda) S_r(\lambda) d\lambda}{\int F_\lambda(\lambda/(1+z)) S_o(\lambda) d\lambda} \right] + Z_o - Z_r, \quad (3)$$

for filter energy sensitivity functions S_r and S_o , with zero points Z_r and Z_o , and SN spectrum F_λ . The time scales t and t' correspond to time after maximum brightness in the observed frame and the SN rest frame, respectively. We computed the K_{ro} using sensitivity functions appropriate to each one of the telescopes and instruments used, together with either a database of well observed and timed spectra of nearby SNe Ia, or the set of representative SN Ia spectra given by Nugent et al. (2002).

The SNe of this campaign were chosen so that their redshifts were close to the redshift at which the observed-frame passbands Rc , Ic , $B45$, and $V45$, are a good match to the rest-frame passbands B and V . This means that the integrals in Eq. (3) are approximately the same, and that their ratio is very close to one. The dependence of the K-correction on the spectral energy distribution of the source is, hence, minimized. This is important in two respects. First, it minimizes the uncertainty in the K-correction (Schmidt et al. 1998; Nugent et al. 2002). Second, it minimizes any time dependence introduced into the observed light curve by the K-correction. The latter is necessary on general grounds, to avoid introducing the time dependence of the nearby SNe Ia (from which the K-corrections are computed) into the distant SN Ia light curves, but also because obtaining the K-correction for distant SNe Ia is an iterative procedure. The K-correction is a function of the intrinsic color of the SN, which is in turn a function of the observed color of the SN and the K-correction. The intrinsic color of the SN depends on the foreground reddening and the speed of the light curve, and both of them vary with the K-correction. The fact that the rest-frame and observed-frame filters match well, however, makes the iteration of the K-corrections almost trivial. The K-correction, the SN light curve, the intrinsic color, and thus the foreground reddening are simultaneously estimated.

Here we used two different light curve fitting methods: the MLCS2k2 method, briefly described by Riess et al. (2004; see Jha, Riess, & Kirshner 2006 for details), and the new PRES method, which is presented by Prieto et al. (2006). The MLCS2k2 is the modern version of the MLCS method of Riess et al. (1998a, 2001). Computation of MLCS2k2 distances was done together with K-corrections from Nugent et al. (2002). The PRES method is a generalization of the Δm_{15} method of Hamuy et al. (1996a) and Phillips et al. (1999). The main idea of the PRES method is to substitute the discrete set of SN light-curve templates by a continuous set of fitting templates built from the discrete set by a weighted-average scheme. The generalization allows a better fit to any observed light curve and, especially, a more straightforward and elegant estimate of the fit uncertainties. Computation of PRES distances was done together with K-corrections as in Kim et al. (1996) and Schmidt et al. (1998), but using a more modern and extensive database with close to 150 spectra of nearby SNe Ia at different phases. The uncertainties in the K-correction are computed from the scatter of K-corrections for different SNe at the same phase.

The two light-curve fitting methods treat foreground reddening in different ways. Before the light-curve fitting, both of the methods correct the observed color for Galactic reddening (Schlegel et al. 1998) as estimated in the direction of each SN. The corrected observed color is the starting value of the iteration used to estimate the host reddening. The MLCS2k2 method uses a Galactic prior for the wavelength dependence of the extinction law, an exponential prior on total extinction, and a Gaussian prior on intrinsic color (see Riess et al. 2004, and

Jha et al. 2006 for further details). SNe with heavy extinction are flagged to avoid systematic errors from different types of dust. In the PRESS method, the host-galaxy reddening is one of the parameters fitted in a standard χ^2 minimization. A Galactic extinction law is used, but no prior on extinction or intrinsic color is assumed.

The fact that the rest-frame and observed-frame filters are a good match implies that the dependence of our K-corrections on SN color was very small. This is good for both methods; it implies that the uncertainty was minimized. Moreover, for MLCS2k2 there were generally only a few iterations between the light-curve fitting and K-correction routines. The resulting SN photometry and K-corrections are given in Tables 9–13, for distances calculated using both the PRES and the MLCS2k2 methods. The light curves fitted using the PRES method are shown in Figure 16. The light-curve fits using MLCS2k2 were similar; they are not shown here. Parameters fitted by the PRES method are given in Table 14, and those fitted by MLCS2k2 in Table 15.

All of the SNe except SN 1999M provided reasonable light-curve fits. An interesting cross-check is the phase that the epoch of maximum light given by the fits implies for the spectra, which can be compared with the phase of the best-matching spectra given in Table 2. The phases provided by the fits are within two days of those implied by the spectra, the exception being again SN 1999M, which gives a mismatch of ~ 4.2 days.

The mismatch of SN 1999M is puzzling. Its light curve appears too broad for a SN Ia, and its color is too red. The PRES method provides a marginally tolerable fit, with large uncertainties in the parameters, while MLCS2k2 fails to provide an acceptable fit. The identification of SN 1999M as a SN Ia seems certain, however, since the spectrum does show the Si II $\lambda 4130$ line. The redshift is secure as well; it was measured through the O II $\lambda 3727$ emission line in the galaxy and shows consistency with the observed shift of the SN features.

With the available data, little can be said of SN 1999M, other than it is clearly an outlier in the known distribution of properties; there is no reasonable match with the nearby SN sample used to calibrate the luminosity versus light-curve shape relations. Given the S/N, the spectrum in Fig. 6 seems normal. The Si II line correlates well with temperature evolution in the ejecta of SNe Ia; its strength in SN 1999M indicates that, close to maximum light, the photospheric temperature was typical. The red color is, hence, correctly interpreted by the light-curve fitting methods as a result of large foreground reddening. Consistent with the very broad light curve is an unusually blue intrinsic color and a high luminosity at maximum. Thus, this appears to have been a very luminous SN, but with large error bars in the calibrated photometry. In comparison with the expectations for the low-mass Λ CDM cosmology, SN 1999M is the most luminous discovered so far by the HZT.

A possible explanation for the SN 1999M mismatch is a problem with one of the images used as templates, in particular the rest-frame V (observations in I_c). SN1999M appeared in a bright host galaxy. If the template subtraction in the observed-frame I_c was flawed, leaving the residual images of the SN with significant galaxy contamination, then the result would be a brighter and redder SN. The best way to test this possibility is to obtain new, high-quality templates and repeat the photometry from the start, a procedure beyond the scope of this work.

4.2. Luminosity Distances

With rest-frame, reddening-free light curves, the luminosities of the distant SNe can be estimated. The comparison of the observed flux, \mathcal{F} , with the luminosity, \mathcal{L} , provides us with luminosity distances,

$$D_L = \left(\frac{\mathcal{L}}{4\pi\mathcal{F}} \right)^{\frac{1}{2}}, \quad (4)$$

and luminosity distance moduli $\mu = m - M$ related to D_L through the definition of magnitude. The distance moduli estimated using the PRES method are included in Table 14, and those estimated using MLCS2k2 in Table 15.

The values of D_L and μ depend on the cosmological parameters, as discussed extensively by Schmidt et al. (1998) for a Λ cosmology and by Garnavich et al. (1998b) for a cosmology with a more general equation of state for the “dark energy.” Comparison of the observed values of μ with those predicted by different cosmologies therefore allows us to set constraints on the cosmological parameters. It is worth stressing that the experiment we describe, the interpretation of the Hubble diagram at high redshift in terms of the dynamical components of the Universe, depends on the evolution of D_L with redshift (i.e., on the ratio of \mathcal{L} to \mathcal{F} in Eq. (4)), and not on the actual value of \mathcal{L} . Thus, our results are independent of the value of the Hubble constant (see discussions in Schmidt et al. 1998; Garnavich et al. 1998b).

5. Discussion

With the distance moduli computed, the SNe Ia can be placed in the high-redshift Hubble diagram that the HZT has been constructing since 1995. In Figures 17 and 18 we present the Hubble diagram for distances determined with the PRES and MLCS2k2 methods, respectively. There is a different number of SNe in each plot, because the two methods use a different low- z SN sample and, in addition, the highest-redshift bins require low- z SNe

with light curves calibrated in the ultraviolet, a passband that has not been incorporated by the PRES method yet. In both the MLCS2k2 and the PRESS methods used here, we have adopted $H_0 = 65 \text{ km s}^{-1} \text{ Mpc}^{-1}$.

All but one of the new SNe provide distances in excess of those expected in an empty universe, usually by a generous amount. SN 1999M, the discrepant event, carries little weight in the Hubble diagram because its distance modulus is either very uncertain (PRES light-curve calibration) or rejected from the light-curve fit (MLCS2k2 light-curve calibration). The weighted average of the PRES luminosity distance moduli for the five new SNe presented here is $42.64 \pm 0.08 \text{ mag}$ at an average redshift of 0.493 ± 0.001 (1σ uncertainties). This is 0.50 mag in excess of the distance modulus that a “cold dark matter” cosmology with $\Omega_M = 0.3$ (and $\Omega_\Lambda = 0$) predicts, a result about 6σ away from this particular expectation. Allowing for the intrinsic dispersion of SN Ia maximum brightness, the expected uncertainty of the five SNe increases to ~ 0.1 (1σ), which is still too small to account for the observed mean difference.

On the one hand, our result is reassuring with respect to some concerns about systematics. It is difficult to imagine *any* systematic effect related to photometry, calibration uncertainty, or evolutionary trends of SNe with lookback time that could give rise to such a large difference. Thus, our results support the conclusion that the expansion of the Universe is currently accelerating.

On the other hand, the average PRES distance modulus is too large to fit comfortably even within the Λ CDM concordance model. If compared with the expectation for a Λ CDM cosmology, with $\Omega_M = 0.3$ and $\Omega_\Lambda = 0.7$, the combined distance modulus of the five SNe is too high by 0.27 mag (i.e., about 3σ away). The discrepancy remains when the calibration using the MLCS2k2 method is considered. The average distance modulus for the four SNe fitted by MLCS2k2 is $42.74 \pm 0.11 \text{ mag}$, which provides an excess of 0.58 mag with respect to the $\Omega_M = 0.3$ and $\Omega_\Lambda = 0.0$ model, a 6σ result. If compared with the currently more realistic Λ CDM model ($\Omega_M = 0.3$, $\Omega_\Lambda = 0.7$), the mean MLCS2k2 luminosity distance is too high by 0.37 mag (nearly 4σ).

Thus, the point in the Hubble diagram with high statistical significance at $z \approx 0.5$ that we sought to establish in this campaign turned out to be challenging. It not only appears inconsistent with a low-mass universe without a cosmological constant, but also with the currently favored concordance Λ CDM cosmology.

The fact that this inference is based on only a handful of SNe does not reduce the impact of this particular campaign in the HZT Hubble diagram. We may consider all the SNe with $0.44 < z < 0.54$ studied by our team to compute a mean distance modulus at $z \approx 0.50$. This

redshift provides the best match between the rest-frame B and observed-frame R_c passbands, thus minimizing the dependence of the K-corrections with the supernova spectrum. As a result, the K-correction is almost constant and its uncertainty is minimized. There are three SNe within this redshift range in Riess et al. (1998a), two in Tonry et al. (2003), two in Barris et al. (2004), and four fitted by MLC2k2 in the present work. The average distance modulus of these eleven SNe, using the calibration provided by MLC2k2, is 42.51 ± 0.07 (1σ uncertainty) at a weighted mean redshift of 0.48. This is, again, long by a generous margin: close to 6σ away from the low-mass universe ($\Omega_M = 0.3$, $\Omega_\Lambda = 0.0$), and almost 3σ in excess of the concordance Λ CDM cosmology ($\Omega_M = 0.3$, $\Omega_\Lambda = 0.7$). Considering only the SNe in Riess et al. (1998a), Tonry et al. (2003), and Barris et al. (2004), the mean distance modulus is 42.39 ± 0.08 (1σ uncertainty), for a weighted mean redshift of, again, 0.48. The latter value is within 1σ of the expectation of the concordance model.

The combined distance moduli of all HZT SNe at $z \approx 0.48$, with and without the SNe presented here, are consistent within 1σ . It is clear, however, that this particular campaign increases the shift to fainter magnitudes in the Hubble diagram at $z \approx 0.5$, implying a stronger acceleration than that of the concordance model.

We fitted the data of figures 17 and 18 with a grid of cosmological models varying Ω_M , Ω_Λ , and H_0 . We computed χ^2/N (where N is the number of degrees of freedom), confirmed as in Tonry et al. (2003) that it is close to unity, then converted the χ^2 distribution to a probability distribution using $\exp(-\chi^2/2)$, normalized the latter, marginalized over H_0 , and found the contours of constant probability that enclose 99.7%, 95.4%, and 68.3% confidence. The procedure is justified in detail by Riess et al. (1998a).

We computed contours for the probability distributions implied by all the HZT SNe Ia in figures 17 and 18, for distances calibrated by both the PRES and the MLCS2k2 methods. We present the results in Figures 19 and 20, for two different samples of the HZT SNe: (a) all of those in Riess et al. (1998a), Tonry et al. (2003), and Barris et al. (2004), and (b) these same SNe plus the new ones reported in this paper. The best-fit parameters for a Λ CDM cosmology resulting from the fits are given in Table 16, for both distance calibration techniques and the different samples considered. In this table, we provide the results of additional fits done with the constraint that $\Omega_M + \Omega_\Lambda = 1$, as suggested most compellingly by the analysis of the WMAP observations (Spergel et al. 2003).

The contours of figures 19 and 20 confirm the results obtained from inspection of the Hubble diagrams. If the fits are left unconstrained, the HZT SNe tend to favor universes with high values of Ω_Λ , but also high values of Ω_M . The new SNe in this campaign push the expected values of both Ω_Λ and Ω_M to somewhat higher values.

The different samples and fitting techniques also give slightly different results. Results from different samples are consistent within the 1σ uncertainty. The different fitting techniques, however, lead to more significant differences, which are due in part to the fact that the SN samples differ in a sensitive way: the more distant SNe Ia in Riess et al. (1998a), Tonry et al. (2003), and Barris et al. (2004) are included in the MLCS2k2 set, but not in the PRES set. Finally, we note that the contours obtained with the MLCS2k2 distances (figure 20) look very similar to the contours of Tonry et al. (2004) (see their Figure 10), even though the SN samples are different.

Rather than thinking in terms of the Ω parameters, which correspond to a definite model of the dynamical components of the Universe, we may simply measure its kinematics through the relation between scale factor and time, represented by redshift and distance moduli, respectively. As already mentioned by Tonry et al. (2003), we then conclude that our SNe suggest a universe that had both substantial deceleration at $z > 0.5$ and unambiguous acceleration more recently. In particular, the SN data for $z \lesssim 1.0$ provide strong evidence that the expansion of the Universe was decelerating at early times (Riess et al. 2004). The low-redshift SNe ($z < 0.5$), of course, provide the best evidence for recent acceleration, as was evident in both the original HZT sample (Riess et al. 1998a) and the SCP sample (Perlmutter et al. 1999). Our results presented here strengthen the case for recent acceleration.

The χ^2 minimum in the elongated direction of the contour ellipses of figures 19 and 20 is shallow. Small-number statistics, as well as systematics present in a given redshift range or in a given search campaign, can easily move the best-fitting Ω values along this direction by a few tenths. The clear shifts of the contours with changes in the sample (in each figure, different line styles correspond to different samples) and with changes in the fitting technique (compare the various figures) illustrate the sensitivity of the results to these issues.

The discrepancy between the results of MLCS2k2 and PRES especially concerns us. To clarify this point, we repeated the computation of contour levels for a sample consisting of exactly the same SN set (92 SNe, 48 of which are in the low- z sample). We do not show the results here because they are redundant: the contours are almost the same as those shown in figures 19 and 20. Thus, it appears that the discrepancy is really due to the different methods used. Further work, already in progress, will help clarify this issue.

The SN sample analyzed here provides an excess distance with respect to the concordance Λ CDM cosmology as large as that given by the sample of Riess et al (1998a) with respect to the empty Universe. Should this be a cause of concern? We think not, mainly for two reasons.

First, the strength of the concordance model comes largely from the convergence of vari-

ous independent experiments that provide consistent expectation values for the cosmological parameters, or for combinations of them. Measuring luminosity distances versus redshift provides a good constraint for combinations of the form $\Omega_\Lambda - \Omega_M$ (Schmidt et al. 1998). It is reassuring to see that, regardless of the chosen sample, the elongated axis of the contour ellipses always crosses the line $\Omega_\Lambda + \Omega_M = 1$ at values consistent with $0.2 < \Omega_M < 0.3$, right in the interval favored by several experiments measuring Ω_M .

Second, the size of the contours and the position of the probability maximum strongly depend both on the number and quality of the SNe Ia in the sample. When the HZT SNe are augmented with those discovered and studied by other programs (see Table 5 in Riess et al. 2004, and references therein), the probability contours shrink, the best-fitting values of both Ω_Λ and Ω_M decrease, and the plot approaches that expected for the concordance model. The presence of several SNe at $z > 1$ is especially important in producing this effect.

Figure 21 shows the results of testing this second assertion. As the number of high-quality SNe using the “gold” sample of Riess et al. (2004) increases, the area enclosed by the confidence contours decreases. In particular, the major axis becomes shorter faster than the minor axis, approaching the minor axis in length; the minimum along the major axis is made deeper by increasing the sample. Moreover, there is a shift of the best-fitting Ω values toward the line $\Omega_\Lambda + \Omega_M = 1$. This suggests that the high values of Ω_Λ and Ω_M implied by the HZT Hubble diagrams of high- z SNe Ia need not be taken too seriously; they are still quite dependent on the sample size, and especially on the number of SNe in the highest-redshift bins.

Even within the limits of the sample, and bearing in mind the differences implied by different fitting techniques, one may ask whether the failure of the Hubble diagrams of various SN subsets to provide best-fitting values of Ω_M and Ω_Λ closer to those expected from the concordance model could be a sign of weakness in the new Λ CDM paradigm. Specifically, perhaps the dark energy is not the cosmological constant, but rather some kind of “quintessence” or rolling scalar field. We explored this question following Garavich et al. (1998b), considering universes with only gravitating matter (Ω_M) and a dark-energy component (Ω_x). We assumed further that the Universe is flat, and that Ω_x can be approximated with an equation of state of the form $P_x = w_x \rho_x c^2$, where P_x and ρ_x are the pressure and density of the dark-energy component. (Note that $w = -1$ if the dark energy is indeed the cosmological constant.) With these elements a new set of models for the luminosity distances can be computed and the predictions compared with the observations. In Figure 22 we show the results of this exercise.

It is not surprising that abandoning the assumption that $w_x = -1$ results in a better fit of the offset of SN distances at $z \approx 0.5$, since there is now a new parameter to adjust.

The interesting fact is that, if we want to fit the SN distances at $z \approx 0.5$, then we need to *decrease* w_x to values significantly smaller than -1 . The best fit gives $w \approx -1.8$, well below that of a cosmological constant. However, matching the luminosity distances at $z \approx 0.5$ with $w_x \approx -1.8$ leads to a bad fit at higher redshifts.

We see that allowing w_x to be a free parameter does not provide the flexibility needed to match the apparently sharp transition in the behavior of luminosity distances with redshift at $z \approx 0.5$. But at this point, our result is only illustrative at best; the samples considered here are not sufficiently large, homogeneous, and well-distributed in redshift to accurately measure w_x . The point of figure 22 is to show that in a low-mass, flat universe, any static value of w_x will fare as badly as $w = -1$ (that is, Λ) in matching the current Hubble diagram of high- z SNe Ia, especially the transition in luminosity distances over the redshift range 0.5–1.0.

In summary, the new SNe Ia presented in this paper support the previous conclusion of the HZT and the SCP that the expansion of the Universe is currently accelerating, consistent with the presence of a cosmological constant or some other form of “dark energy.” It is encouraging to see that, as the number of SNe increases, the contours of the HZT Hubble diagram, as well as those of other collaborations, become tighter and more consistent with the “concordance Universe.” However, to make further progress, we need more SNe, better light curves, more reliable spectroscopic classifications, and more accurate K-corrections. As the samples grow, decreasing scatter caused by the intrinsic dispersion in luminosity and by observational uncertainties, proper attention to systematic errors will become paramount. In particular, it will become pressing to obtain a better understanding of the entire SN Ia phenomenon. This understanding will be needed on many fronts to test the empirical calibrations that we so confidently extrapolate at high redshifts: from theoretical studies of the progenitors, their evolutionary path to the explosive state, and the explosion itself, to detailed analytical studies of nearby and progressively more distant SN samples.

We thank the staffs of the many facilities we used for their assistance with the observations. Financial support for this work was provided by NASA through grants GO-08177, GO-08641, and GO-09118 from the Space Telescope Science Institute, which is operated by the Association of Universities for Research in Astronomy, Inc., under NASA contract NAS 5-26555. Funding was also provided by National Science Foundation grants AST-0206329, AST-0307894, and AST-0443378. A.C. acknowledges the support of CONICYT (Chile) through FONDECYT grants 1980803, 1000524, and 7000524, as well as the Directors of CTIO and MSSSO for support during periods of work in La Serena and Canberra, respectively. A.V.F. is grateful for a Miller Research Professorship at UC Berkeley during which part of this work was completed.

REFERENCES

- Afshordi, N., Loh, Y.-S., & Strauss, M. S. 2004, *Phys. Rev. D*, 69, 083524
- Aguirre, A. 1999a, *ApJ*, 512, 19
- Aguirre, A. 1999b, *ApJ*, 525, 583
- Alard, C., & Lupton, R. H. 1998, *ApJ*, 503, 325
- Allen, S. W., Schmidt, R. W., Ebeling, H., Fabian, A. C., & van Speybroeck, L., 2004, *MNRAS*, 352, 1365
- Barris, B., et al. 2004, *ApJ*, 602, 571
- Bahcall, N., et al., 2003, *ApJ*, 585, 182
- Bertin, E., & Arnouts, S. 1996, *A&AS*, 117, 393
- Boughn, S., & Crittenden, R. 2004, *Nature*, 427, 45
- Carroll, S. M. <http://www.livingreviews.org/Articles/Volume4/2001-1carroll/>
- Clocchiatti, A. et al., 2000, *ApJ*, 529, 661
- Cousins, A. W. J. 1976, *Mem. R. Astron. Soc.*, 81, 25
- de Bernardis, P., et al. 2002, *ApJ*, 564, 559
- Dolphin, A. E. 2000, *PASP*, 112 1397
- Dolphin, A. E. 2003, http://www.stsci.edu/hst/HST_overview/documents/calworkshop/workshop2002/CW2002_Papers/CW02_dolphin
- Fosalba, P., et al. 2003, *ApJ*, 597, L89
- Garnavich, P. M., et al. 1998a, *ApJ*, 493, L53
- Garnavich, P. M., et al. 1998b, *ApJ*, 509, 74
- Garnavich, P. M., et al. 1999, *IAU Circ.* 7097
- Germany, L. M. 2001, Ph.D. Dissertation, Australian National University
- Hamuy, M., Phillips, M. M., Maza, J., Suntzeff, N. B., Schommer, R. A., & Avilés, R. 1995, *AJ*, 109, 1

- Hamuy, M., Phillips, M. M.,
Hamuy, M., et al. 1996a, AJ, 112, 2408 Suntzeff, N. B., Schommer, R. A., Maza, J., Smith,
R. C., Lira, P., & Avilés, R. 1996b, AJ, 112, 2438
Holtzman, J. A., et al. 1995, PASP, 107, 1065
Jha, S. 2002, Ph.D. Dissertation, Harvard University
Jha, S., Riess, A. G., & Kirshner, R. P. 2006, submitted
Johnson, H. L., 1955, Annu. Astrophys., 18, 292
Kirshner, R. P., et al., 1993, ApJ415, 589
Kennicutt, R. C., 1992, ApJS, 79, 255
Kim, A., Goobar, A., & Perlmutter, S. 1996, PASP, 108, 190
Knop, R., et al. 2003, ApJ, 598, 102
Kron, G. E., & Smith, J. L. 1951, ApJ, 113, 324
Landolt, A. U. 1992, AJ, 104, 340
Leibundgut, B., Tammann, G. A., Cadonau, R., & Cerrito, D. 1991, A&ASuppl., 89, 537
Leibundgut, B. 2001, ARA&A, 39, 67
Nolta, M. R., et al. 2004, ApJ, 608, 10
Nugent, P., Kim, A., & Perlmutter, S. 2002, PASP, 114, 803
Oke, J. B., et al., 1995, PASP, 107, 375
Peacock, J. A., et al. 2001, Nature, 410, 169
Perlmutter, S., & Schmidt, B. P. 2003, Phys. Rev. Lett., 598, 195
Perlmutter, S., et al. 1995, ApJ, 440, 41
Perlmutter, S., et al. 1998, Nature, 391, 51
Perlmutter, S., et al. 1999, ApJ, 517, 565
Phillips, M. M. 1993, ApJ, 413, L105

- Phillips, M. M., Lira, P., Suntzeff, N. B., Schommer, R. A., Hamuy, M., & Maza, J. 1999, *AJ*, 118, 1766
- Prieto, J. L., et al. 2006, submitted to *ApJ*
- Richmond, M., et al., *AJ*, 109, 2121
- Riess, A. G. 2000, *PASP*, 112, 1284
- Riess, A. G., Press, W. H., & Kirshner, R. P. 1995, *ApJ*, 438, 17
- Riess, A. G., Press, W. H., & Kirshner, R. P. 1996, *ApJ*, 473, 88.
- Riess, A. G., et al. 1997, *AJ*, 114, 722
- Riess, A. G. et al. 1998a, *AJ*, 116, 1009
- Riess, A. G., Nugent, P., Filippenko, A. V., Kirshner, R. P., Perlmutter, S. 1998b, *ApJ*, 504, 935
- Riess, A. G., et al. 2000, *ApJ*, 536, 62
- Riess, A. G., et al. 2001, *ApJ*, 560, 49
- Riess, A. G., et al. 2004, *ApJ*, 607, 665
- Schlegel, D. J., Finkbeiner, D. P., & Davis, M. 1998, *ApJ*, 500, 525 (SFD)
- Schmidt, B. P., et al. 1998, *ApJ*, 507, 46
- Scranton, R., et al. 2005, submitted to *Phys. Rev. Letters* (astro-ph/0307335)
- Spergel, D. N., et al. 2003, *ApJS*, 148, 175
- Suntzeff, N. B., et al. 2006, in preparation
- Tonry, J., et al. 2003, *ApJ*, 594, 1
- Wittman, D. M., Tyson, J. A., Bernstein, G. M., Lee, R. W., dell’Antonio, I. P., Fischer, P., Smith, D. R., & Blouke, M. M. 1998, *Proc. SPIE*, 3355, 626

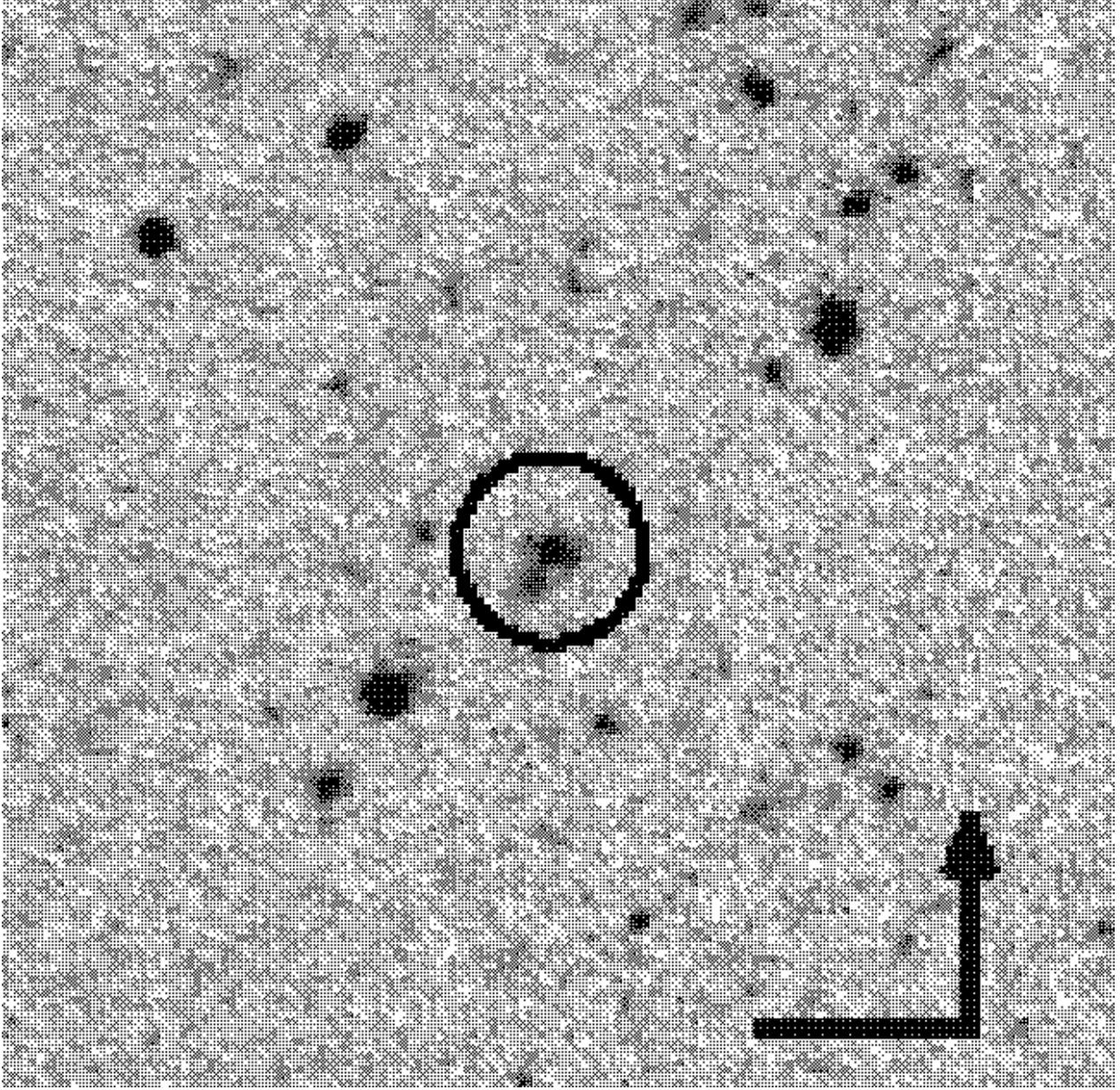


Fig. 1.— Finder chart for SN 1999M. This is the discovery image taken with the CTIO 4.0 m telescope on 1999 Jan. 13, through an R_c filter. SN 1999M is centered in the circle. The width of the image shown is $\sim 66''$. North (up) and east (left) are indicated by the arrow and line, respectively.

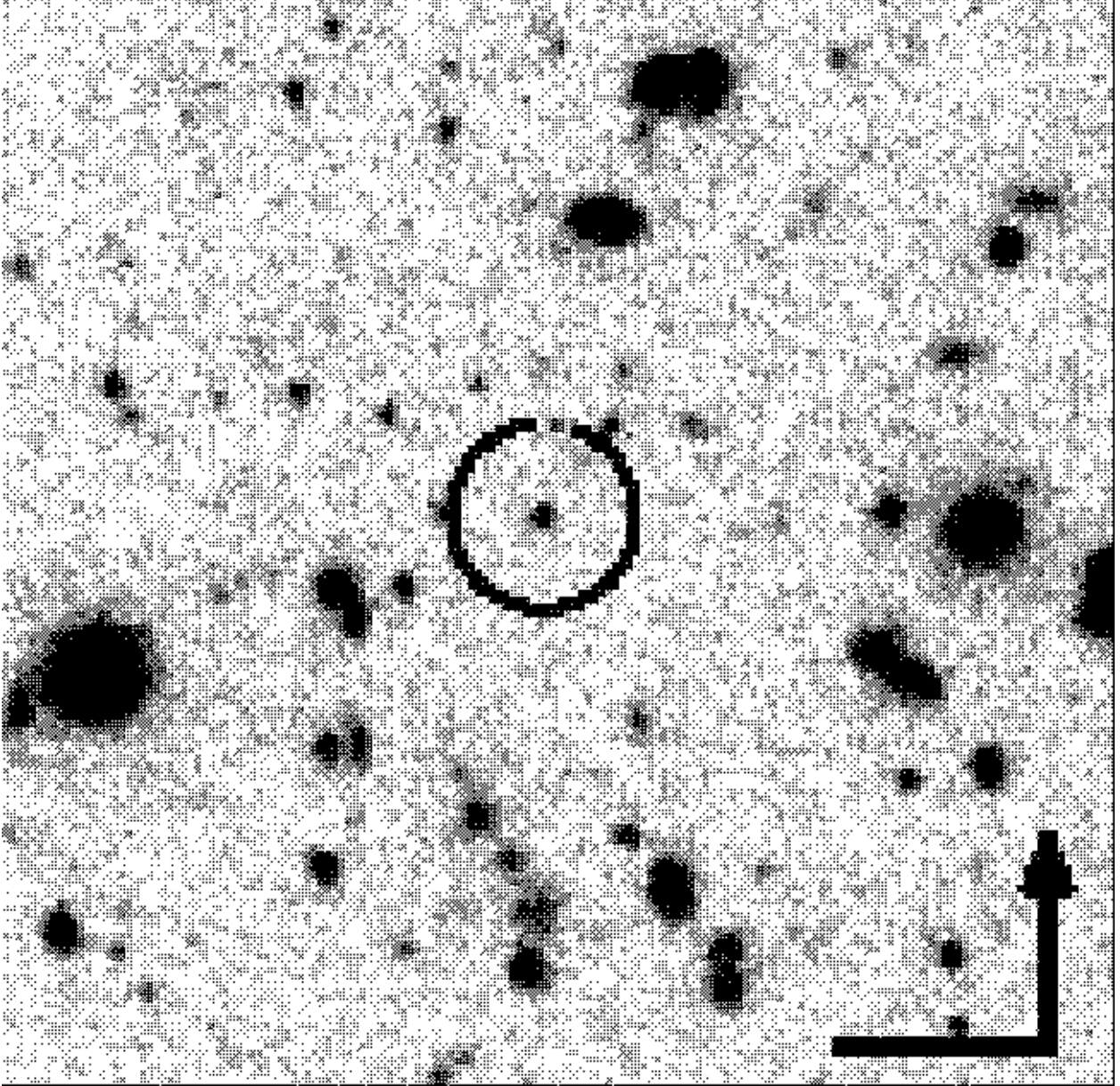


Fig. 2.— Finder chart for SN 1999N, obtained on 1999 Jan. 13. See Figure 1 for other details.

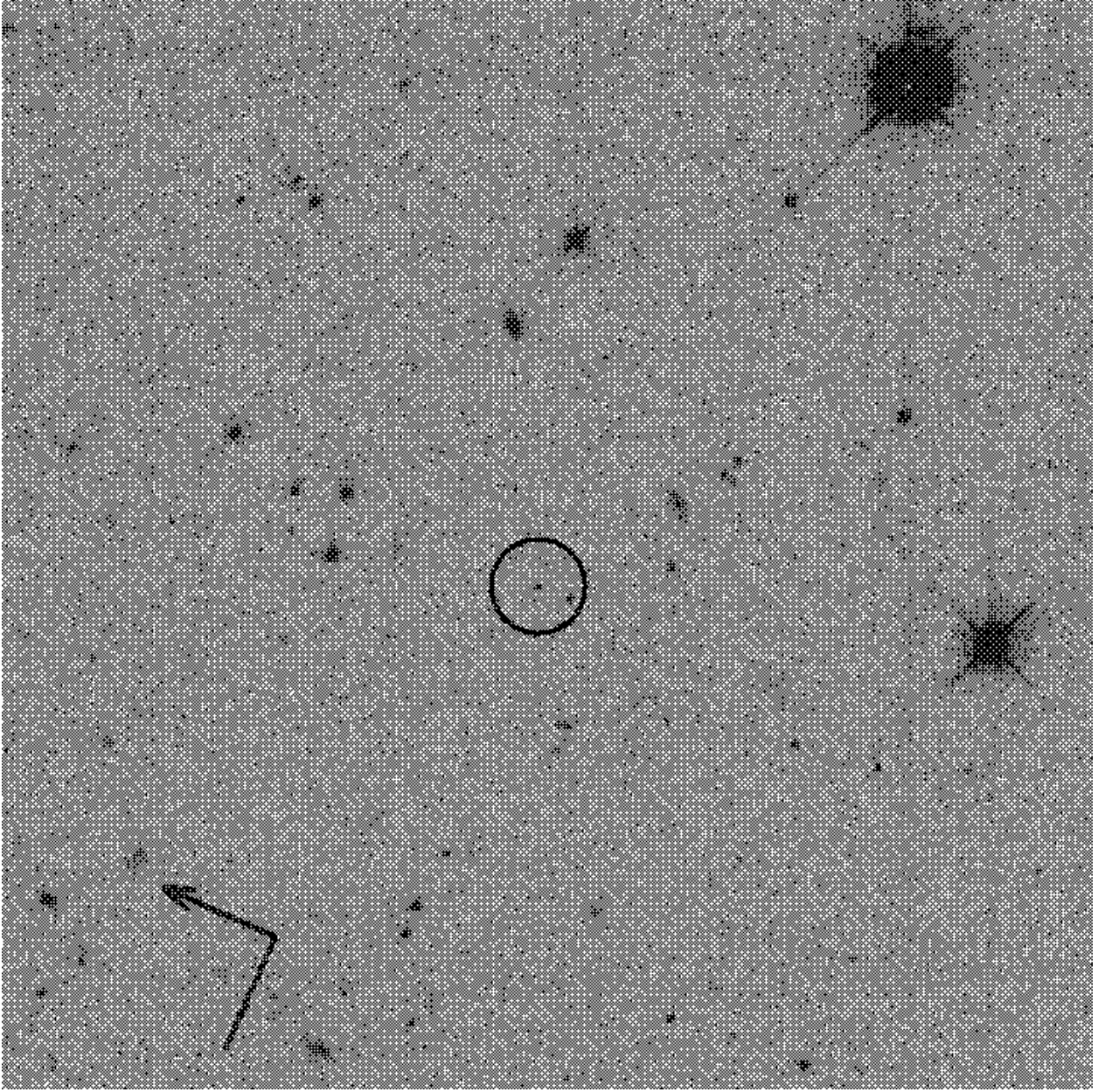


Fig. 3.— Finder chart for SN 1999Q. The image is a combination of 6 *HST* WFPC2 images taken through filter F675W, between 1999 Feb. 1 and 1999 Mar. 7. SN 1999Q is centered in the circle. The width of the image shown is $\sim 66''$. North and east are indicated by the arrow and line, respectively, near the bottom-left corner of the image.

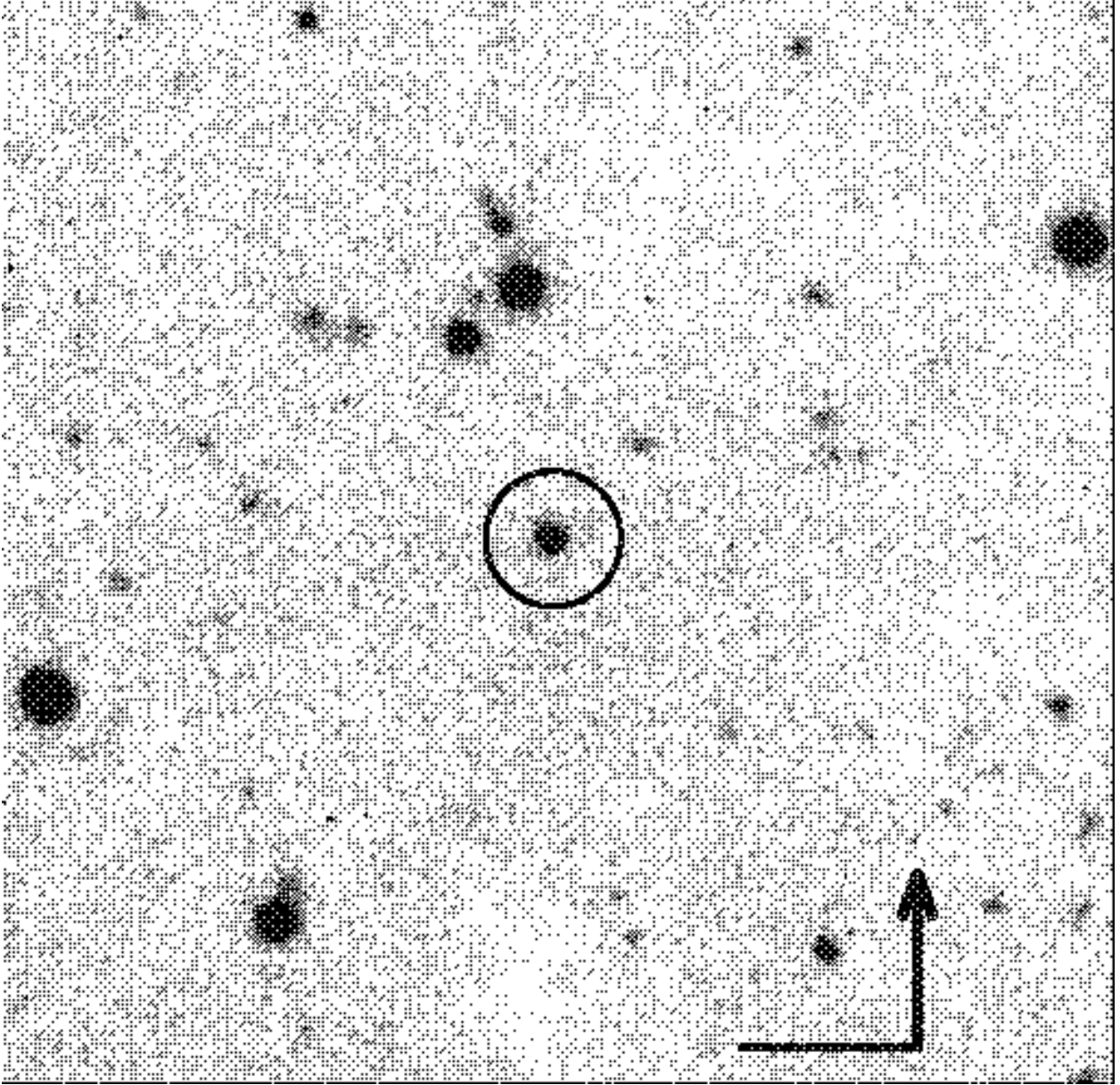


Fig. 4.— Finder chart for SN 1999S. This *R*-band image was obtained on 1999 Feb. 9 with LRIS on the Keck-2 telescope. SN 1999S is centered in the circle. The width of the image shown is $\sim 66''$. North (up) and east (left) are indicated by the arrow and line, respectively.

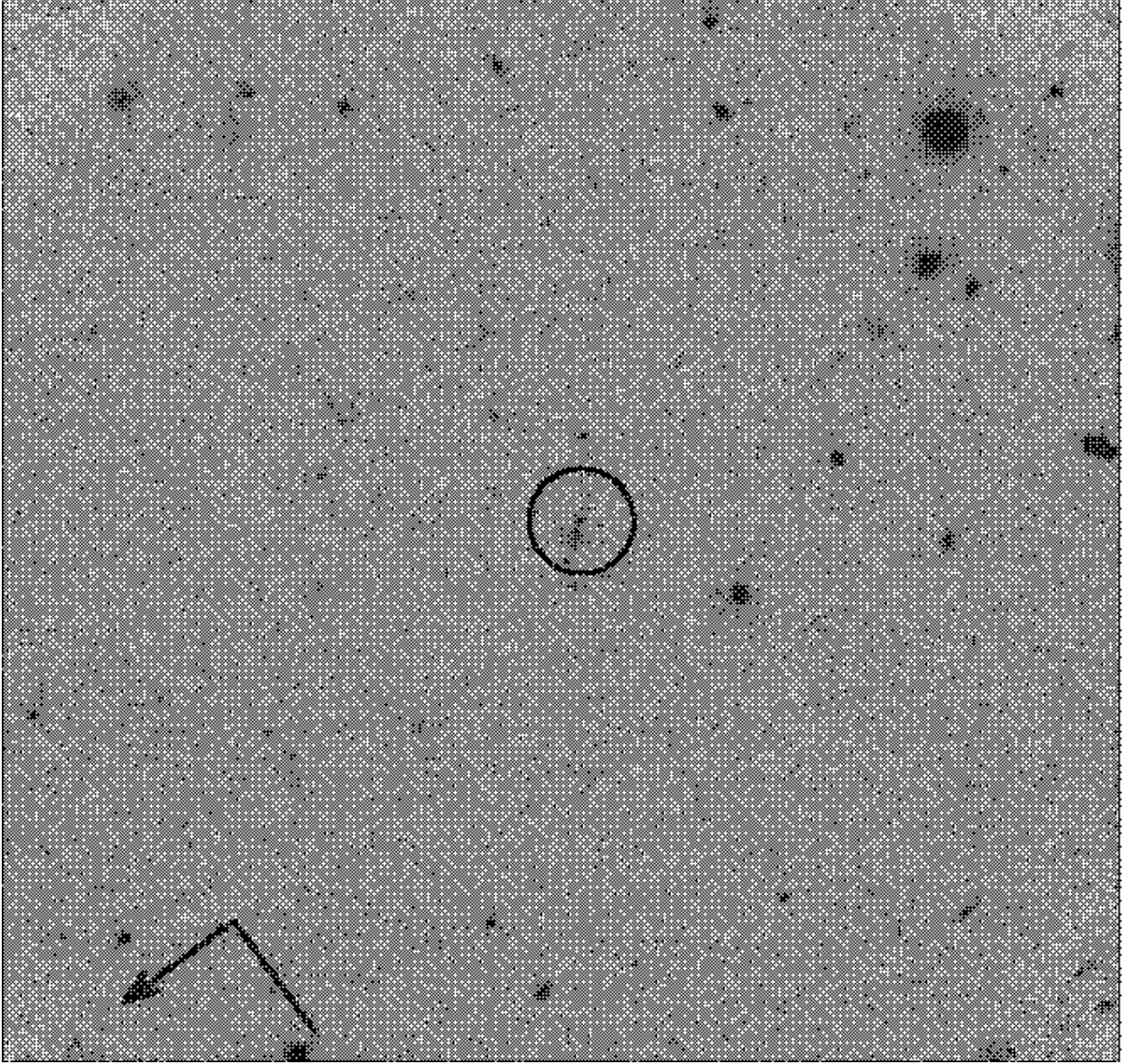


Fig. 5.— Finding chart for SN 1999U. The picture shows a combination of 6 *HST* WFPC2 images taken through filter F675W, between 1999 Feb. 1 and 1999 Mar. 7. See Figure 3 for other details.

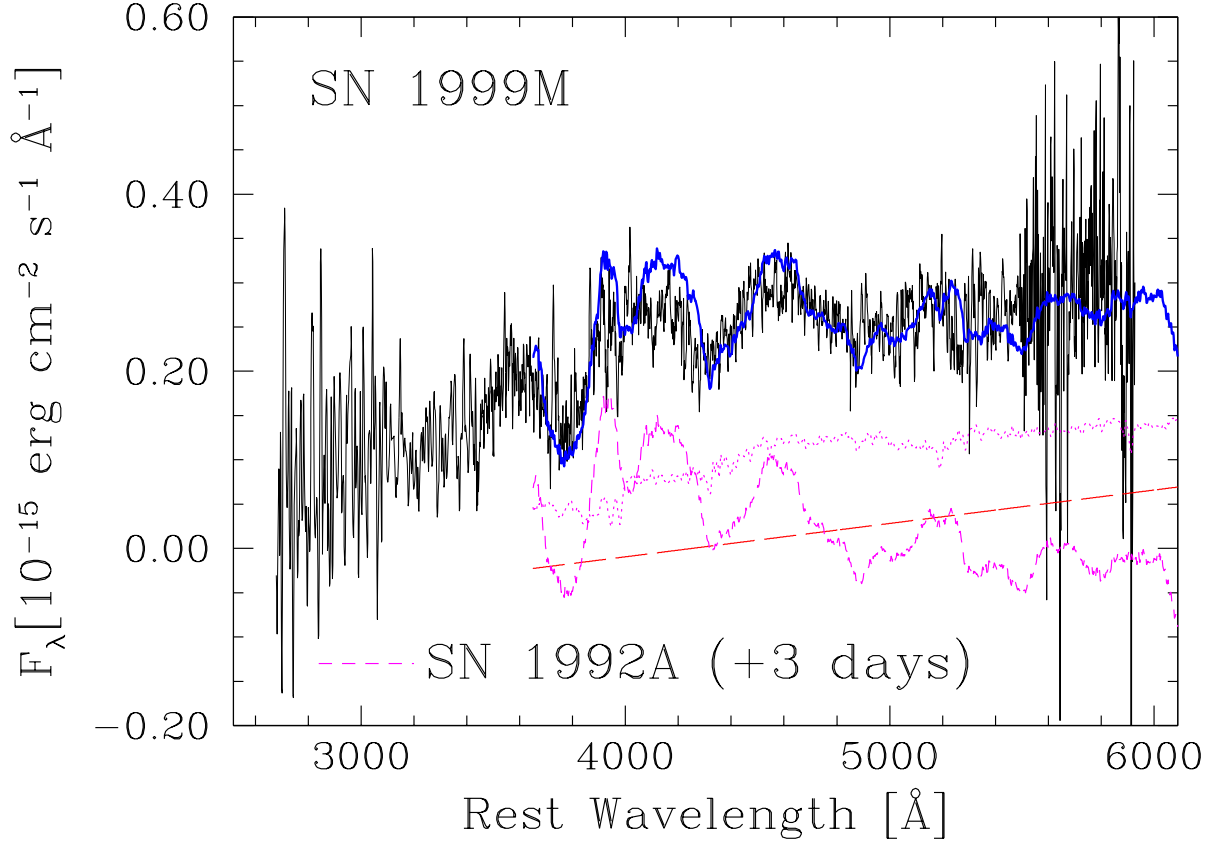


Fig. 6.— Keck-1 spectrum of SN 1999M (thin solid line). The long dashed line shows the unknown slope (see text). The short dashed line give the nearby SN spectrum taken as a model. The dotted line is the spectrum of the contaminating galaxy. The SN model spectrum is SN 1992A, 3 days after B maximum (Kirshner et al. 1993). The thick solid line is the combination of the nearby SN, galaxy, and slope. All spectra have the units indicated along the ordinate, with the exception of the isolated spectrum of SN 1992A, which has been shifted by an additive constant for clarity.

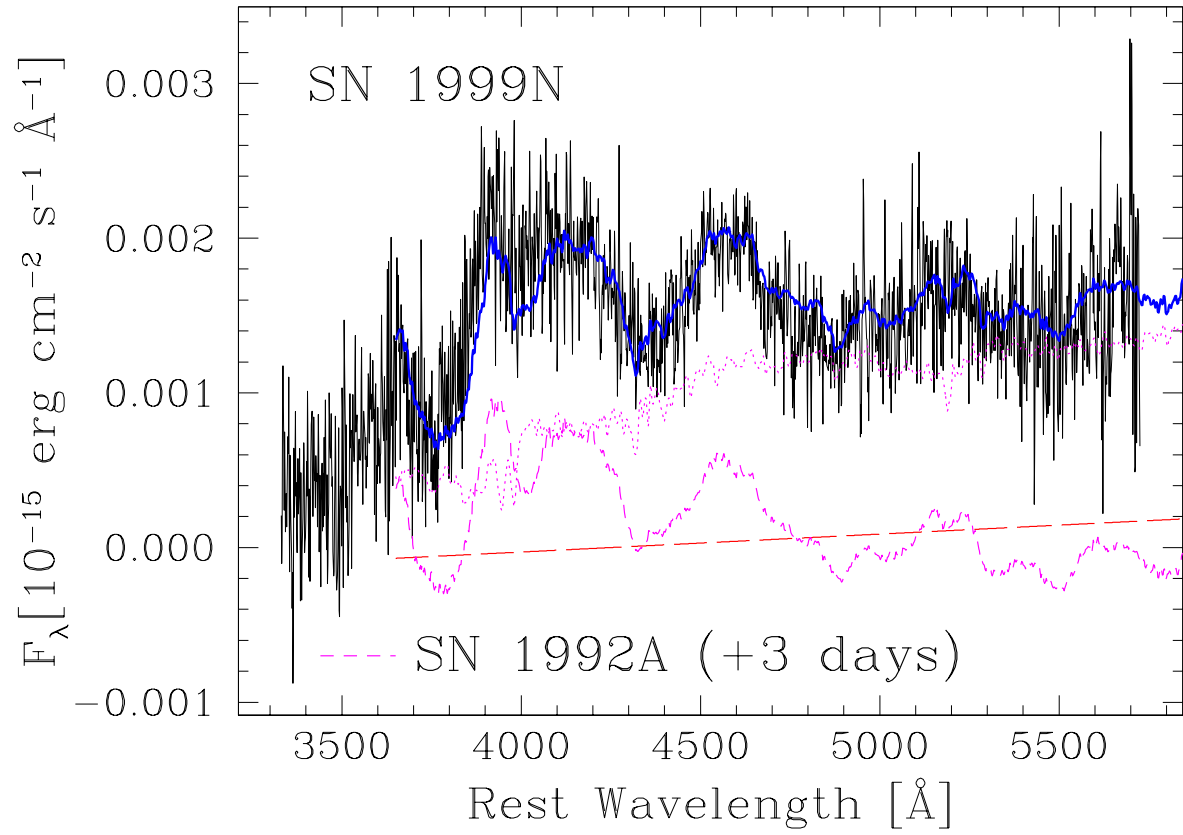


Fig. 7.— Keck-1 spectrum of SN 1999N. Elements are the same as in Figure 6, although the flux scale is different.

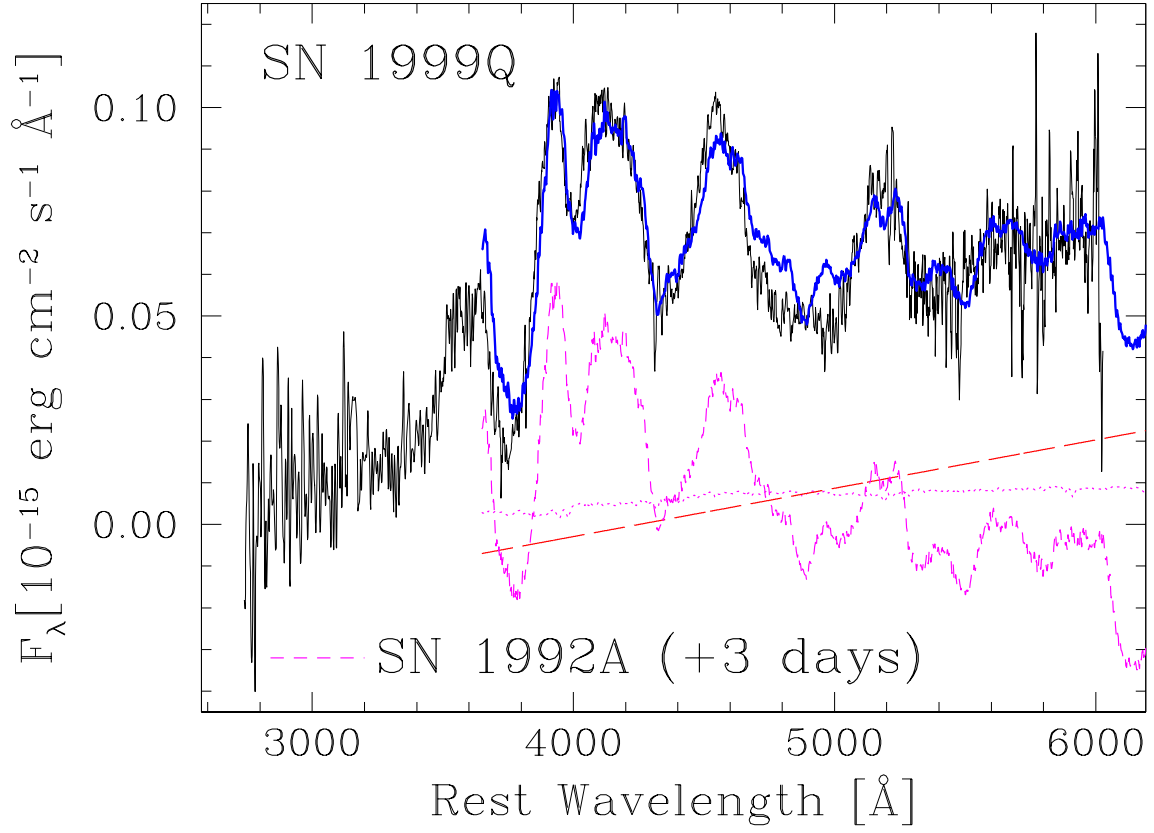


Fig. 8.— Keck-1 spectrum of SN 1999Q. Elements are the same as in Figure 6, although the flux scale is different. Of the SNe in our sample, this one is the least contaminated by the host galaxy.

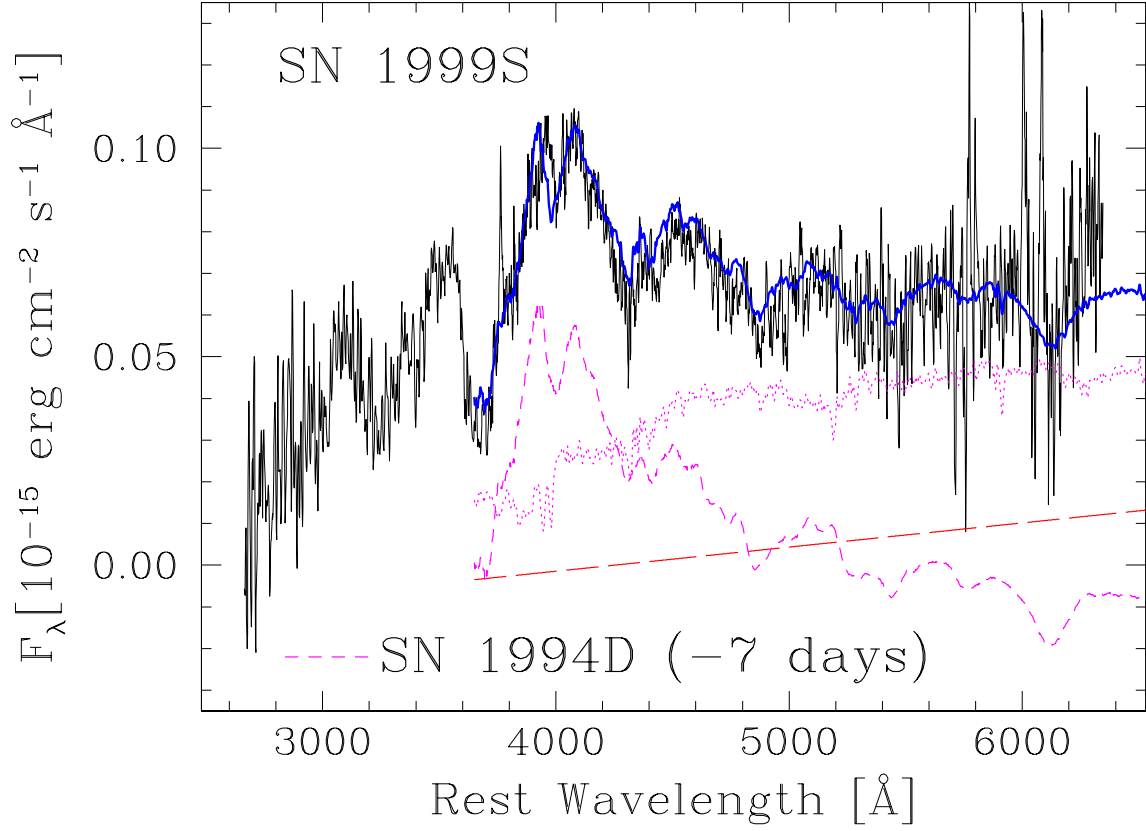


Fig. 9.— Keck-1 spectrum of SN 1999S. Elements are the same as in Figure 6, although the flux scale is different. The SN model spectrum in this case is SN 1994D, 7 days before B maximum (Richmond et al. 1995).

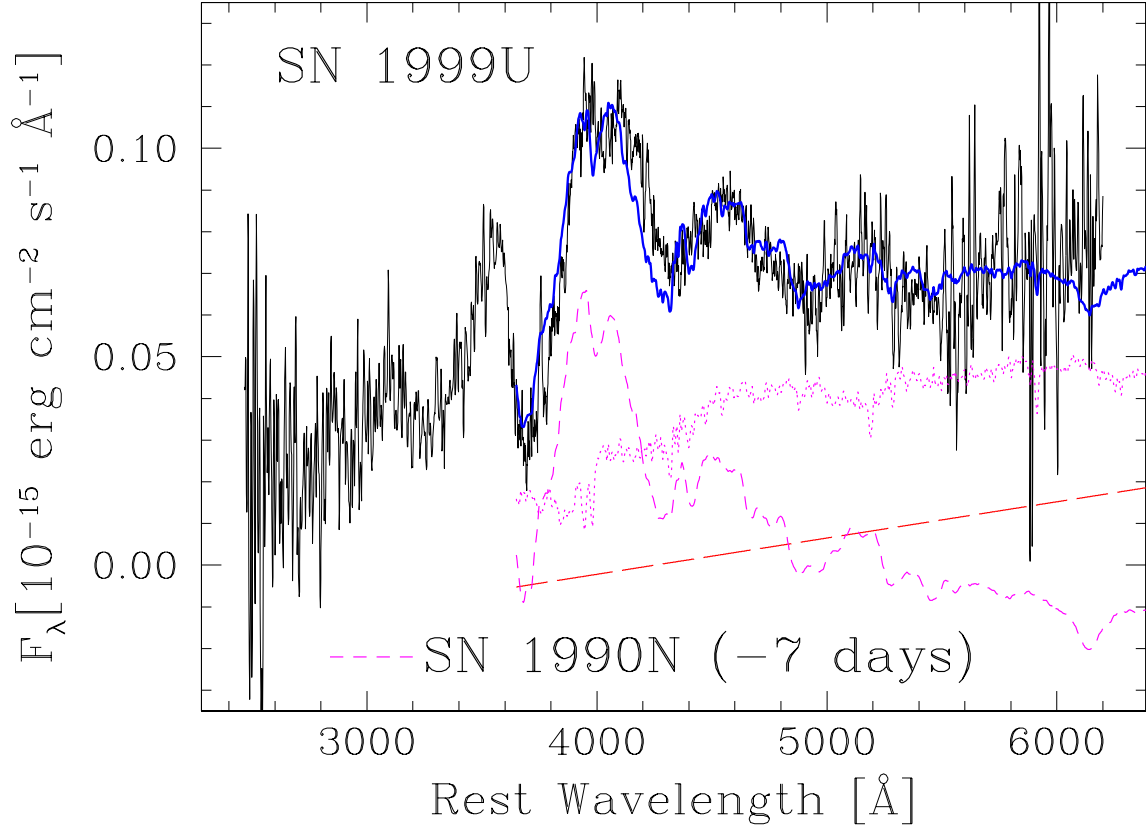


Fig. 10.— Keck-1 spectrum of SN 1999U. Elements are the same as in figure 6, although the flux scale is different. The SN model spectrum in this case is SN 1990N, 7 days before B maximum (Leibundgut et al. 1991).

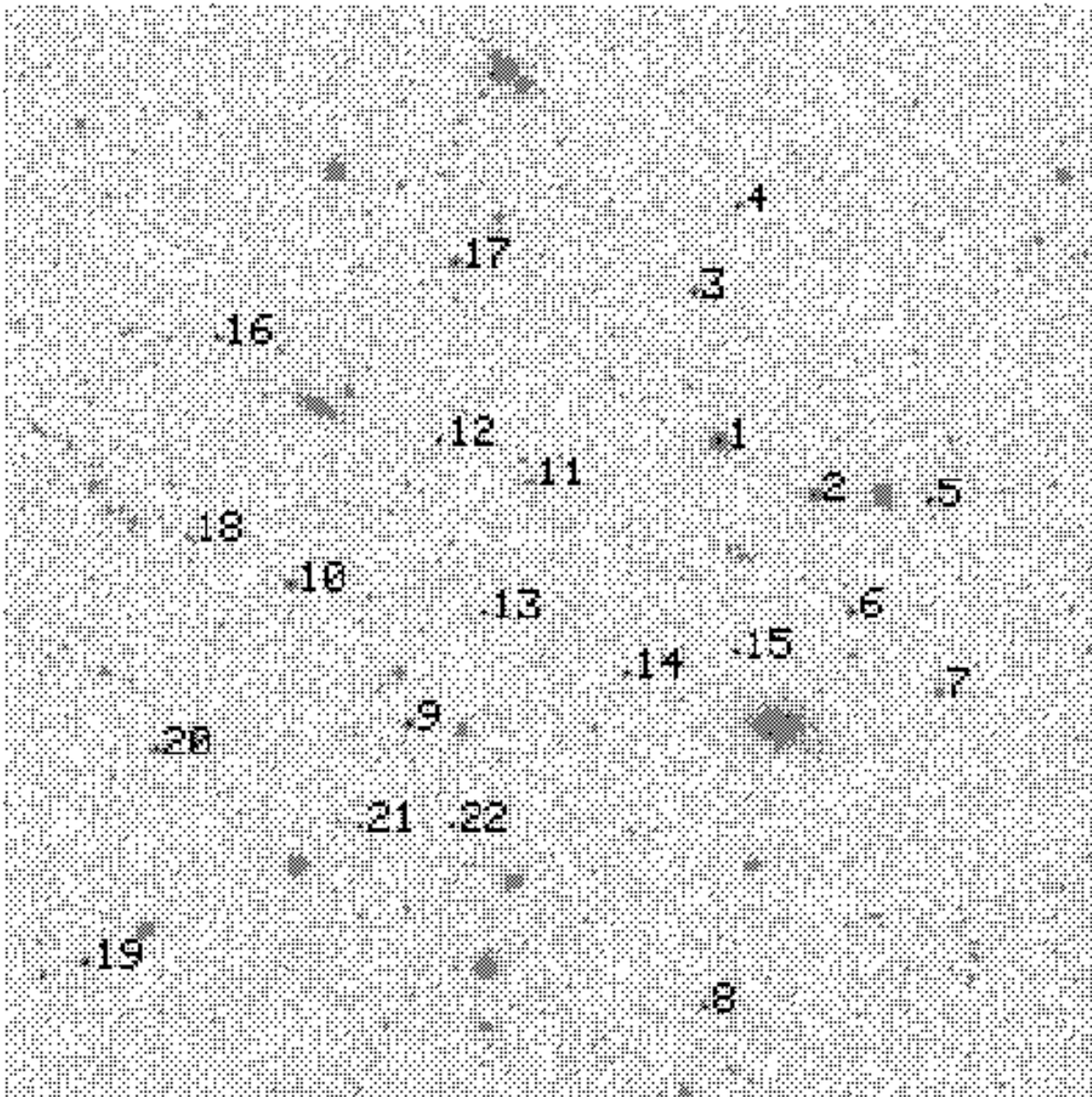


Fig. 11.— Sequence of local standard stars in the field of SN 1999M. North is up, east is to the left. The field of view is $\sim 11'$ wide. The image was obtained with the CTIO 1.5 m telescope through an R_c filter, on 1999 Feb. 19.

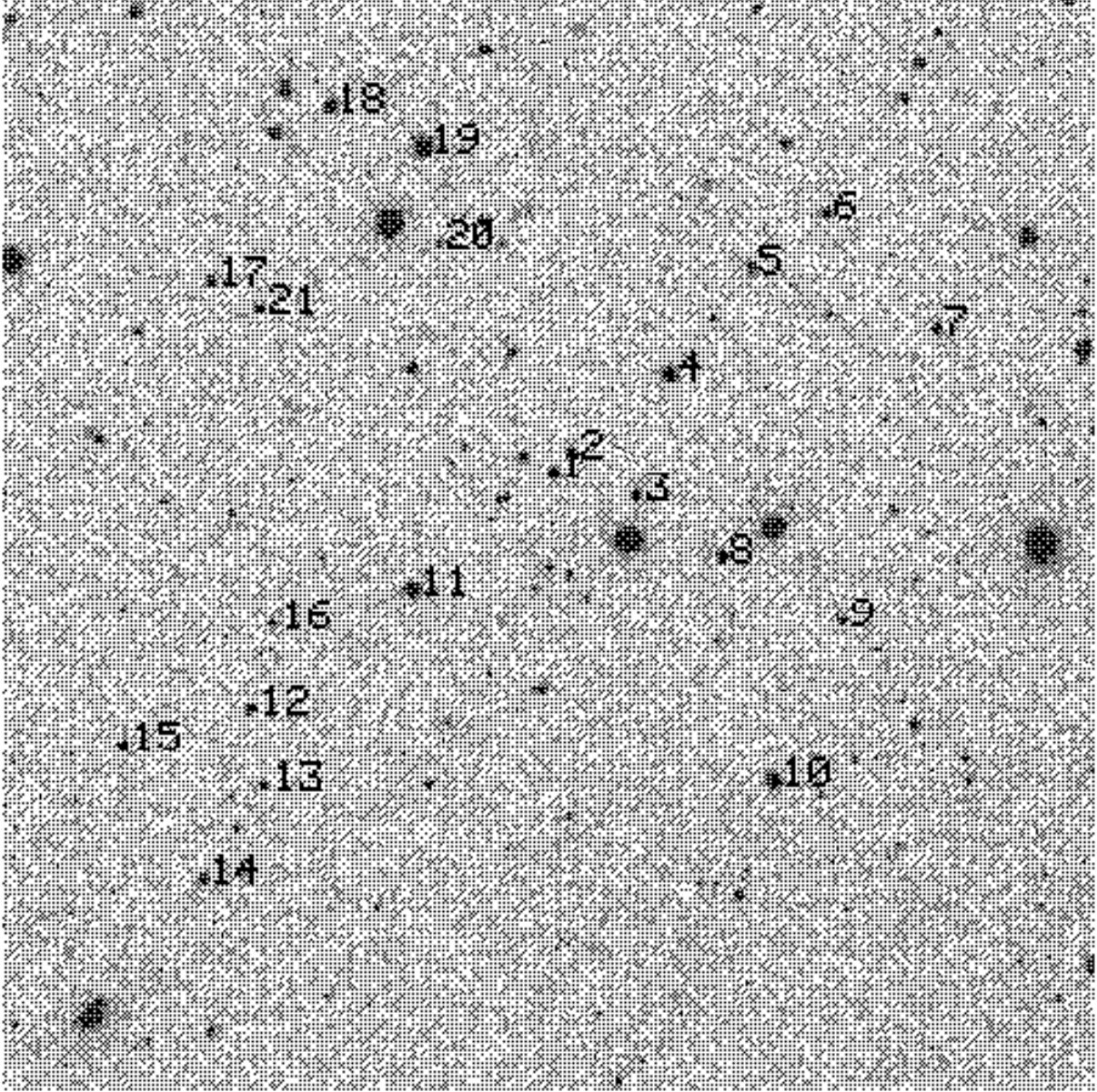


Fig. 12.— Sequence of local standard stars in the field of SN 1999N. North is up, east is to the left. The field of view is $\sim 11'$ wide. The image was obtained with the CTIO 1.5 m telescope through an R_c filter on 1999 Feb. 19.

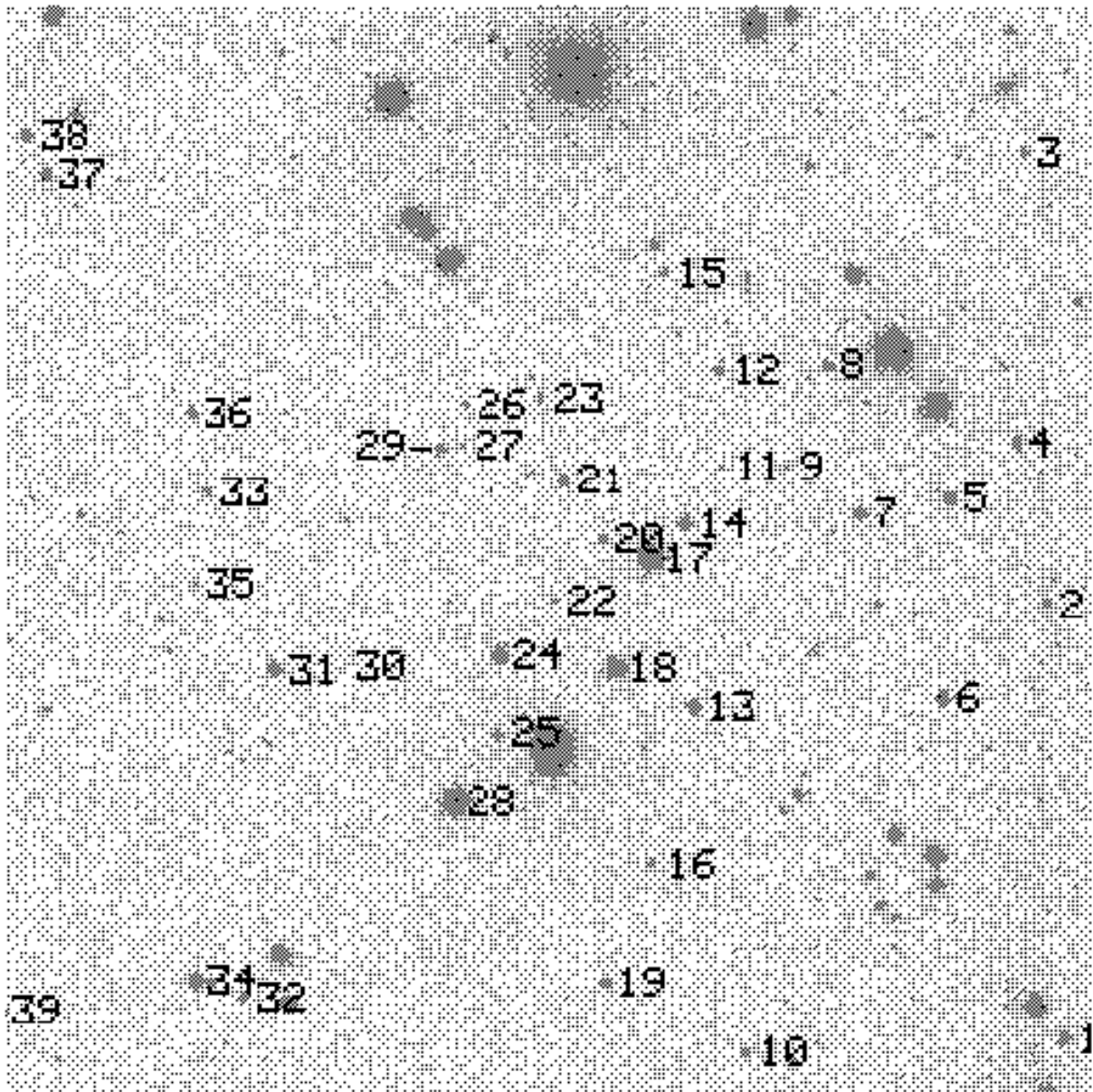


Fig. 13.— Sequence of local standard stars in the field of SN 1999Q. North is up, east is to the left. The field of view is $\sim 11'$ wide. The image was obtained with the CTIO 1.5 m telescope through an I_c filter on 1999 Feb. 18.

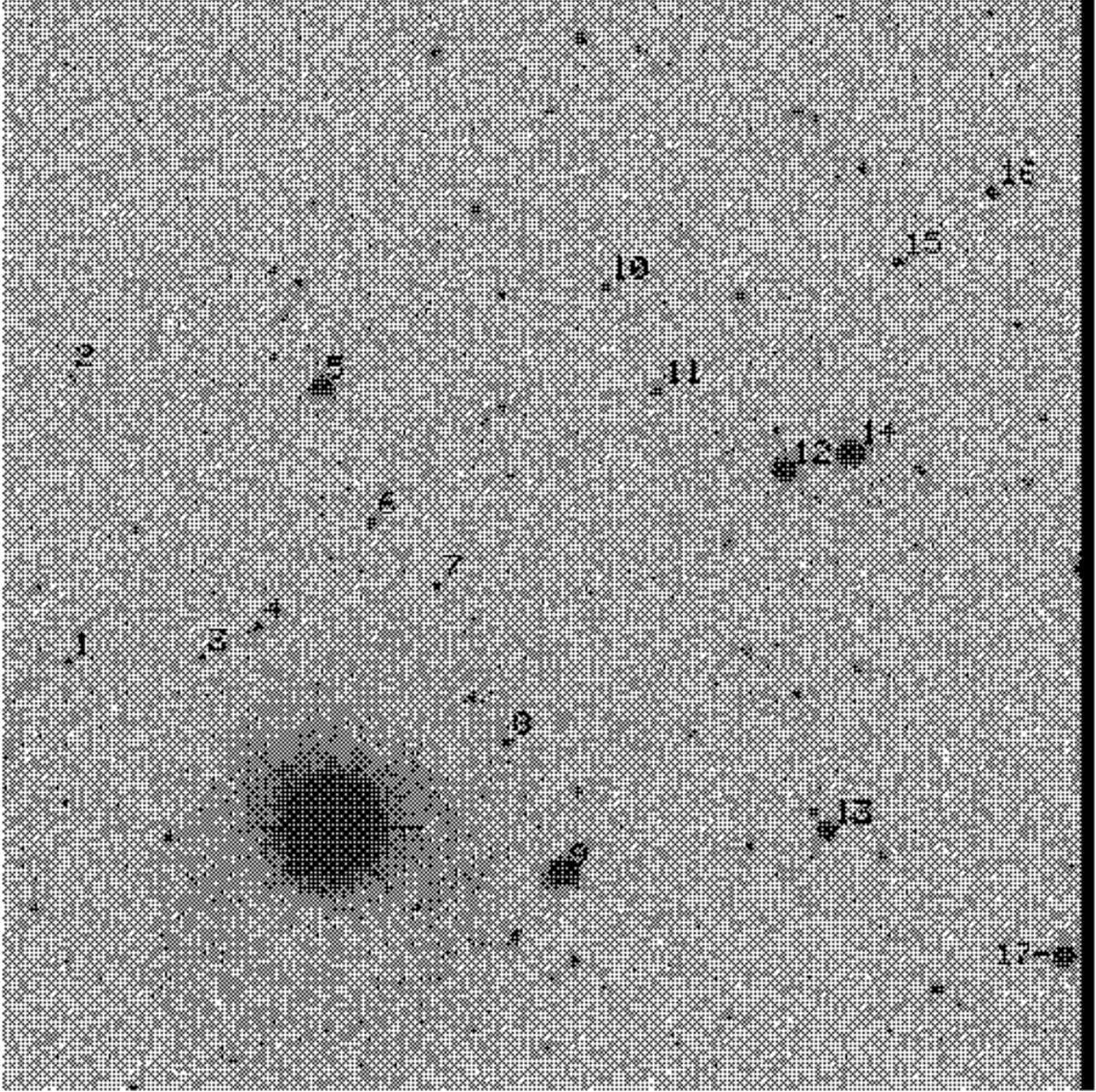


Fig. 14.— Sequence of local standard stars in the field of SN 1999S. North is up, east is to the left. The field of view is $\sim 11'$ wide. The image was obtained with the CTIO 1.5 m telescope through an R_c filter on 1999 Feb. 19.

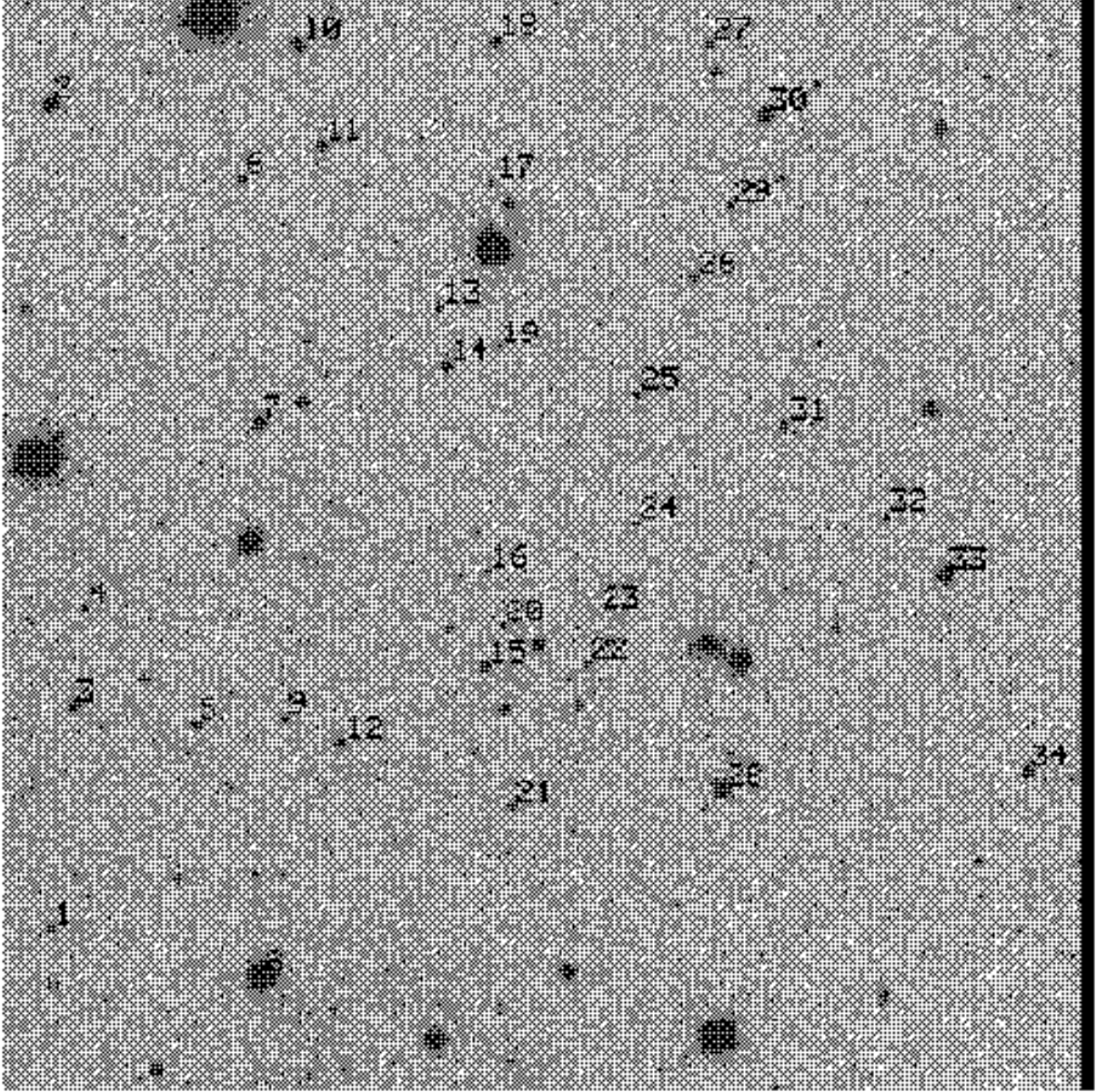


Fig. 15.— Sequence of local standard stars in the field of SN 1999U. North is up, east is to the left. The field of view is $\sim 11'$ wide. The image was obtained with the CTIO 1.5 m telescope through an R_c filter on 1999 Jan. 20.

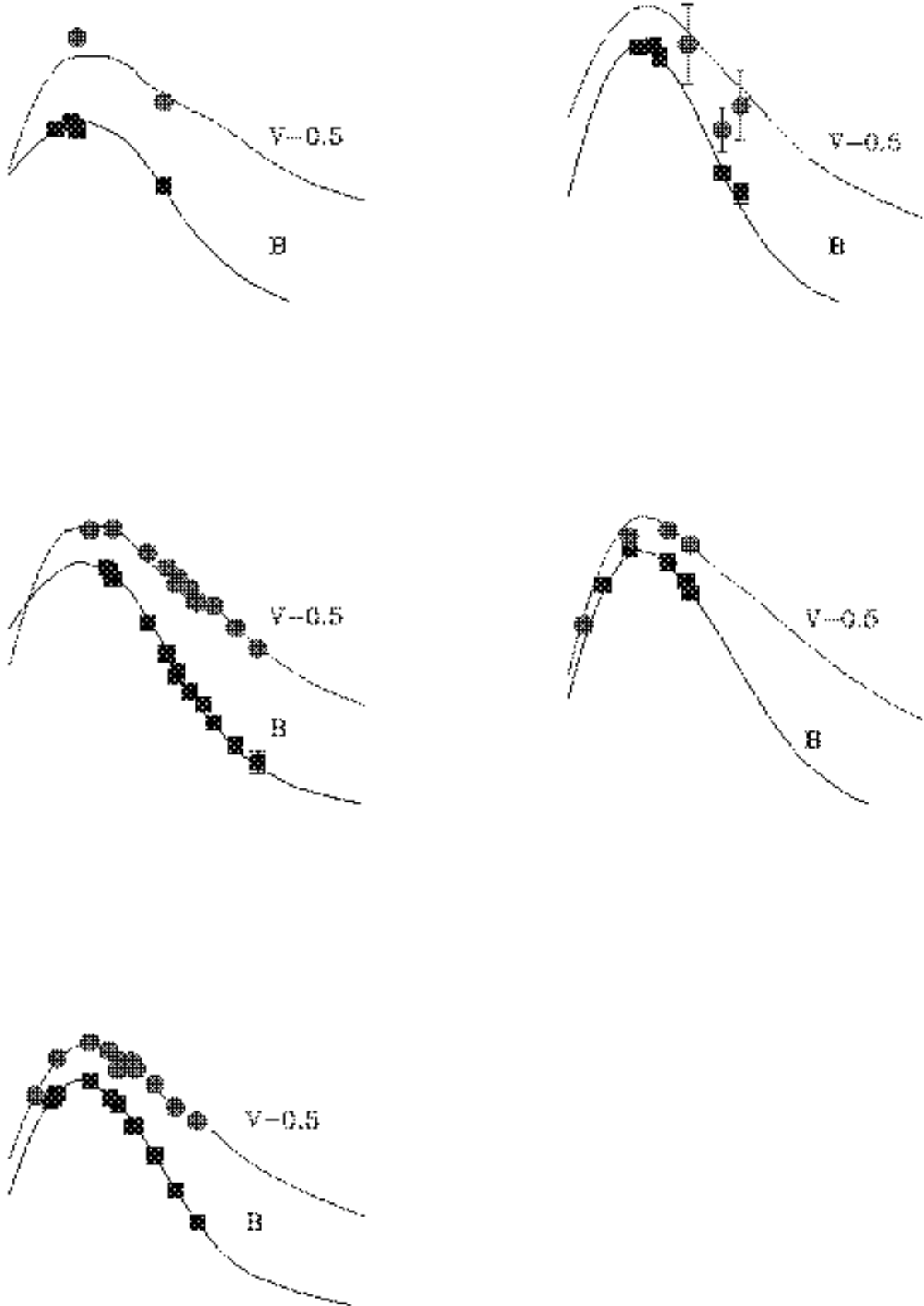


Fig. 16.— SN light curves fitted using the PRES method. The error bars correspond to 1σ . Where error bars are not visible, they are smaller than the plotting symbol.

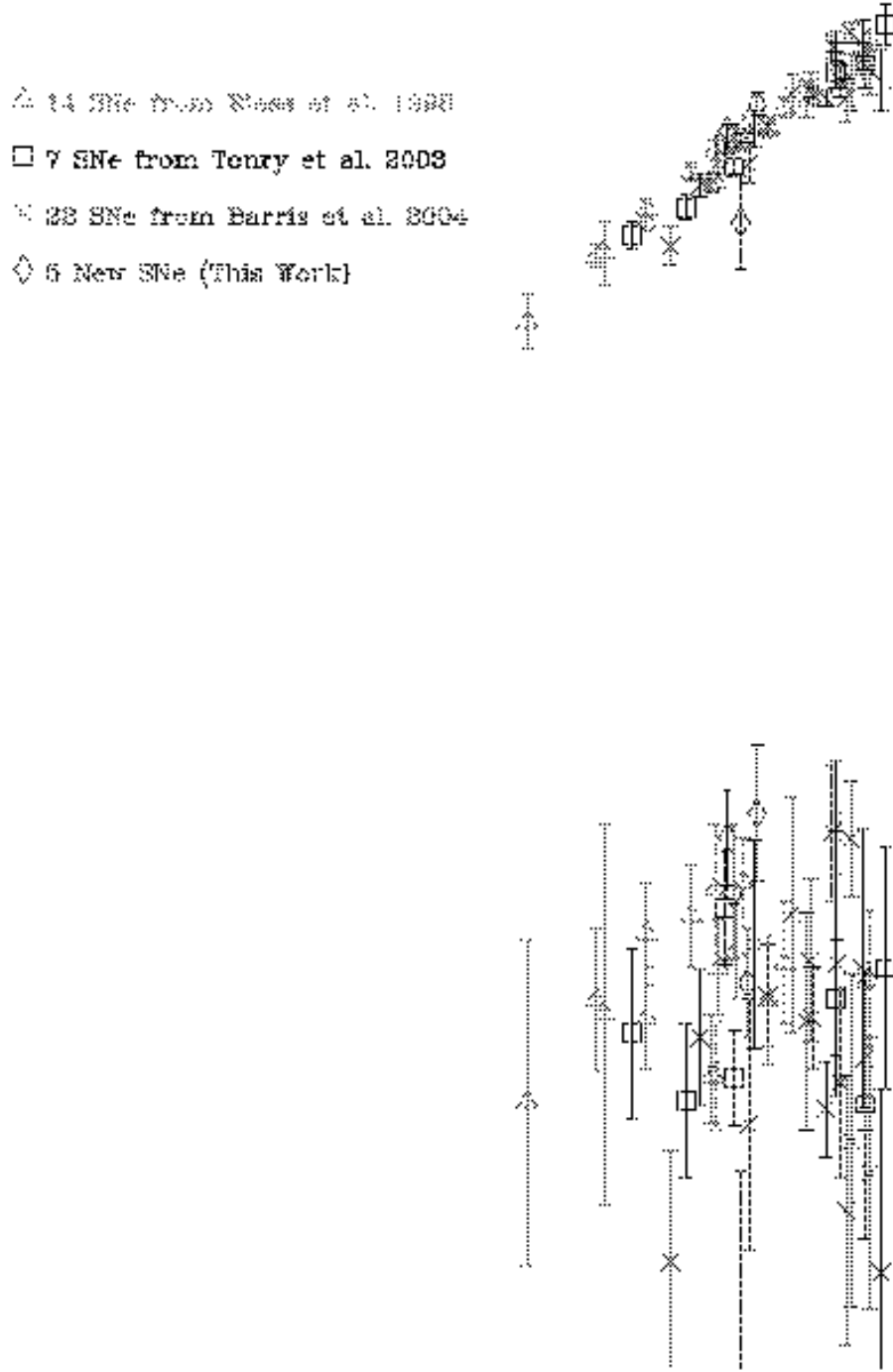


Fig. 17.— Hubble diagram of the HZT SNe (this work, plus Riess et al. 1998, Tonry et al. 2003, and Barris et al. 2004). Error bars are 1σ . Models corresponding to the luminosity distances for a variety of parameters, as indicated, have been plotted. The lower panel, with the same line style key, shows a differential Hubble diagram, where the ordinate corresponds to the difference between a given distance modulus and that in an empty universe.

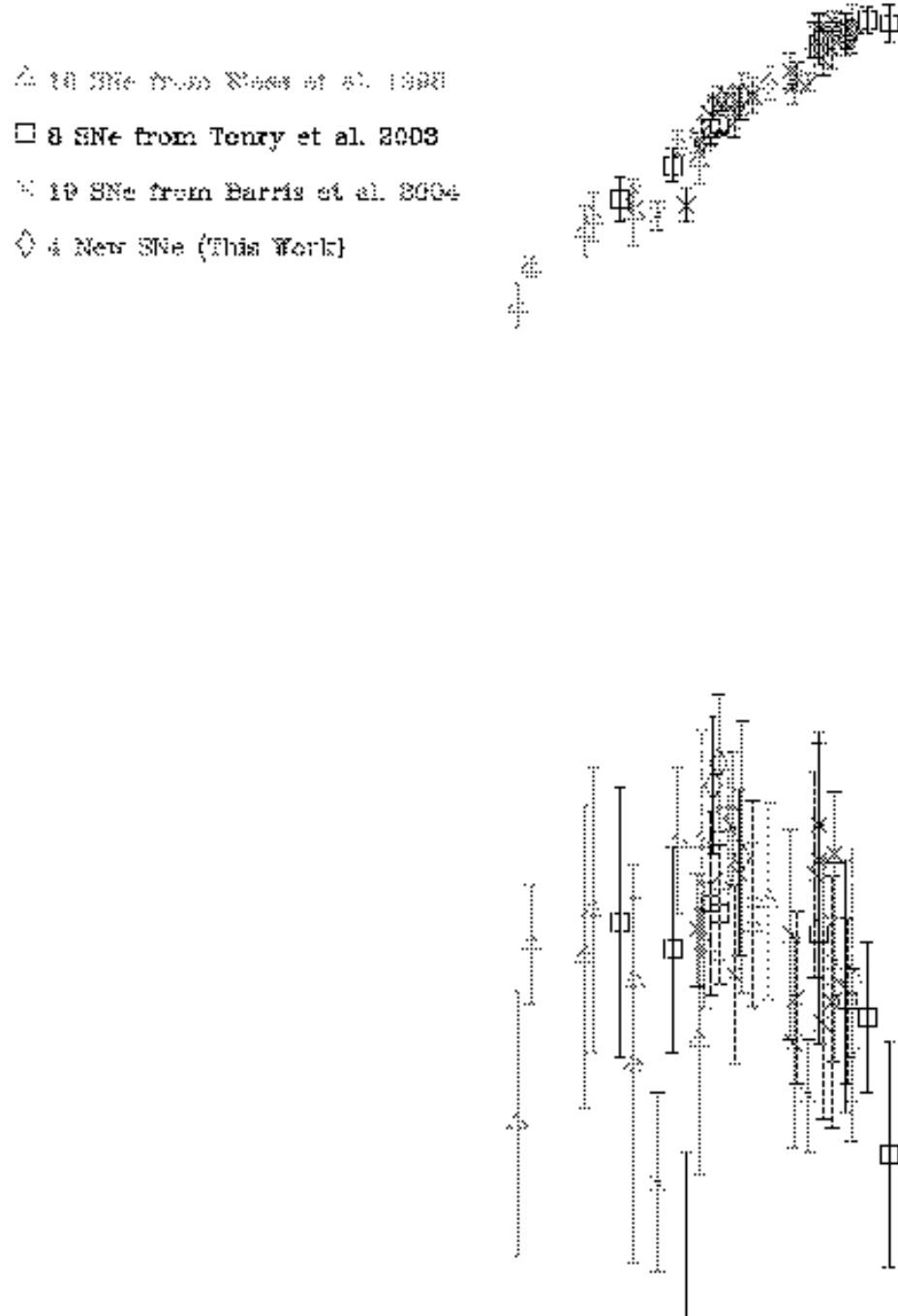


Fig. 18.— The same as Figure 17, but now for the distances calibrated using MLCS2k2.

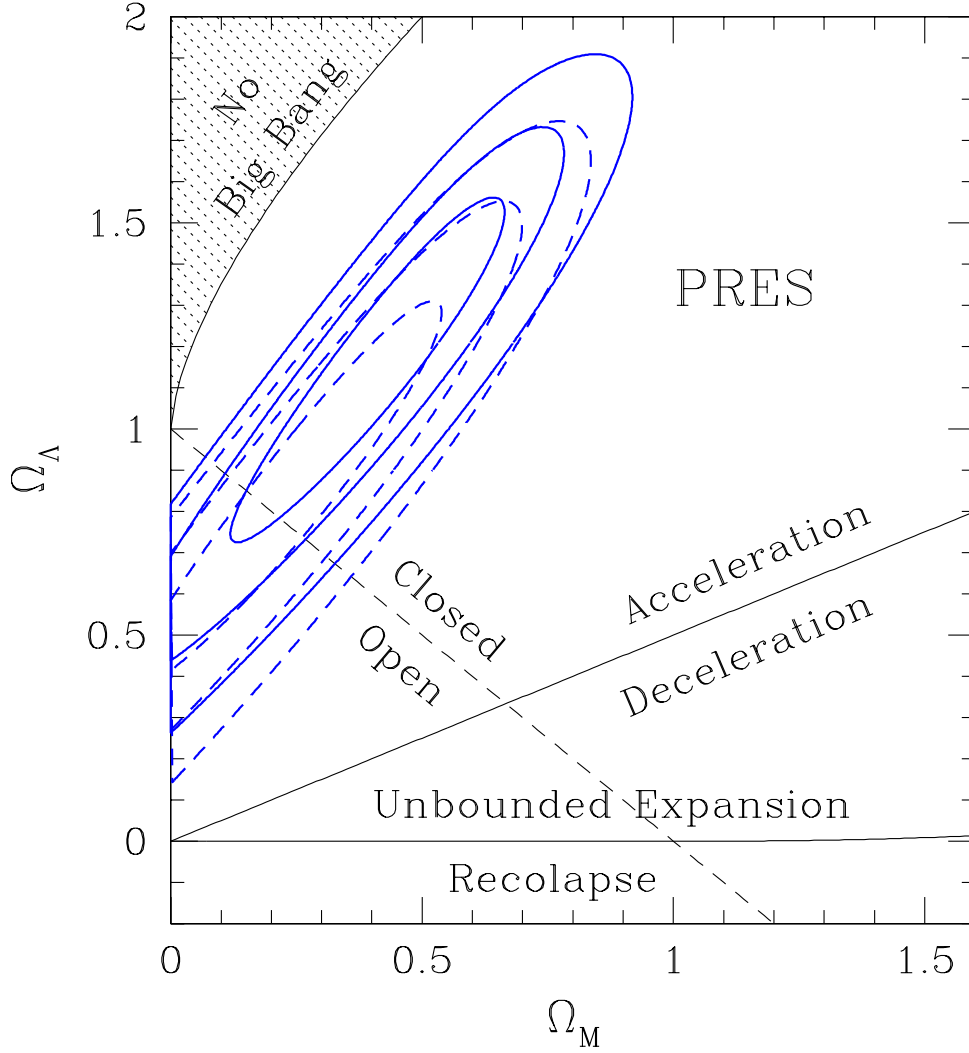


Fig. 19.— Joint probability contours for the parameters Ω_Λ and Ω_M that best fit the Hubble diagram of Figure 17 (distances calibrated using the PRES method). From larger to smaller, the contours drawn correspond to 99.5%, 97%, and 68% confidence, respectively. Continuous lines show the contours corresponding to all the HZT SNe for which a PRES light curve can be fitted. Dashed lines correspond to the subset presented in Riess et al. (1998), Tonry et al. (2003), and Barris et al. (2004) (i.e., this campaign excluded). The best-fitting parameters are given in Table 16.

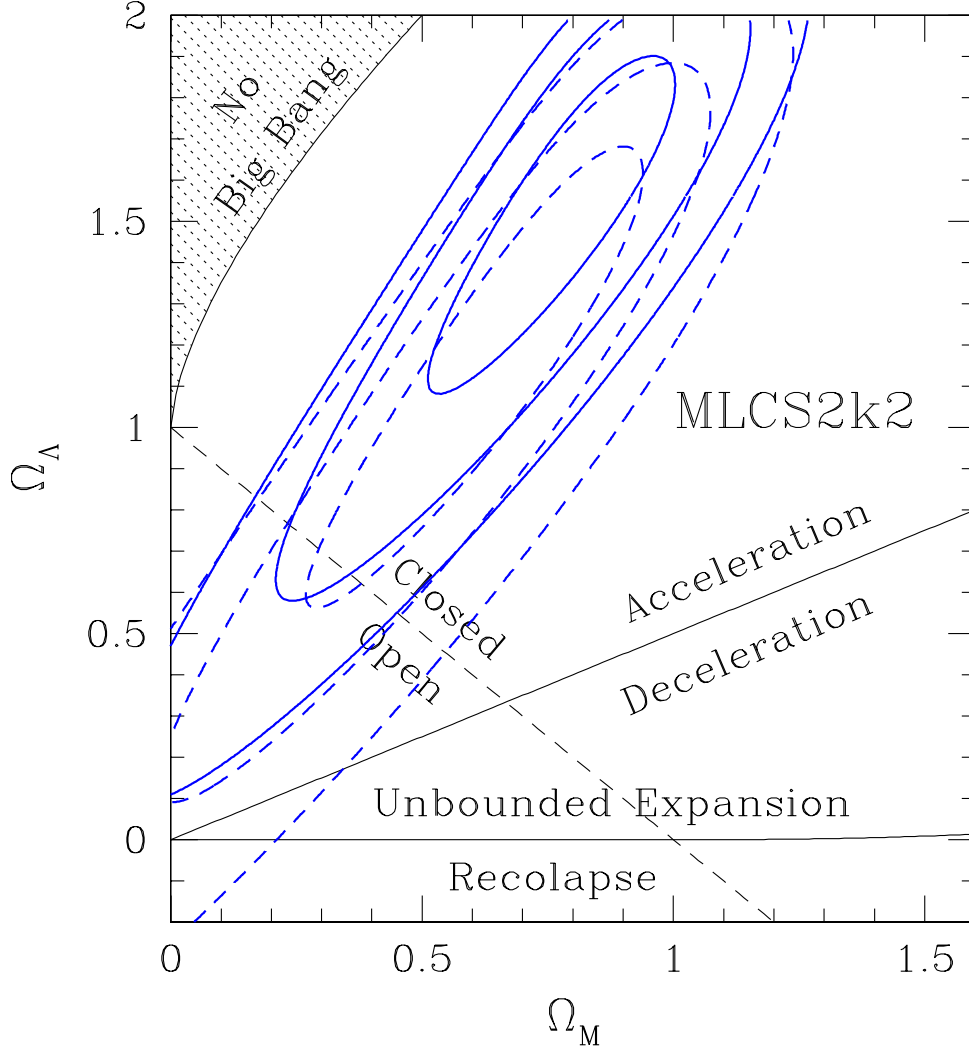


Fig. 20.— The same as figure 19, but now the probability contours were fitted using the Hubble diagram of Figure 18 (with distances calibrated using MLCS2k2). The best-fitting parameters are given in Table 16.

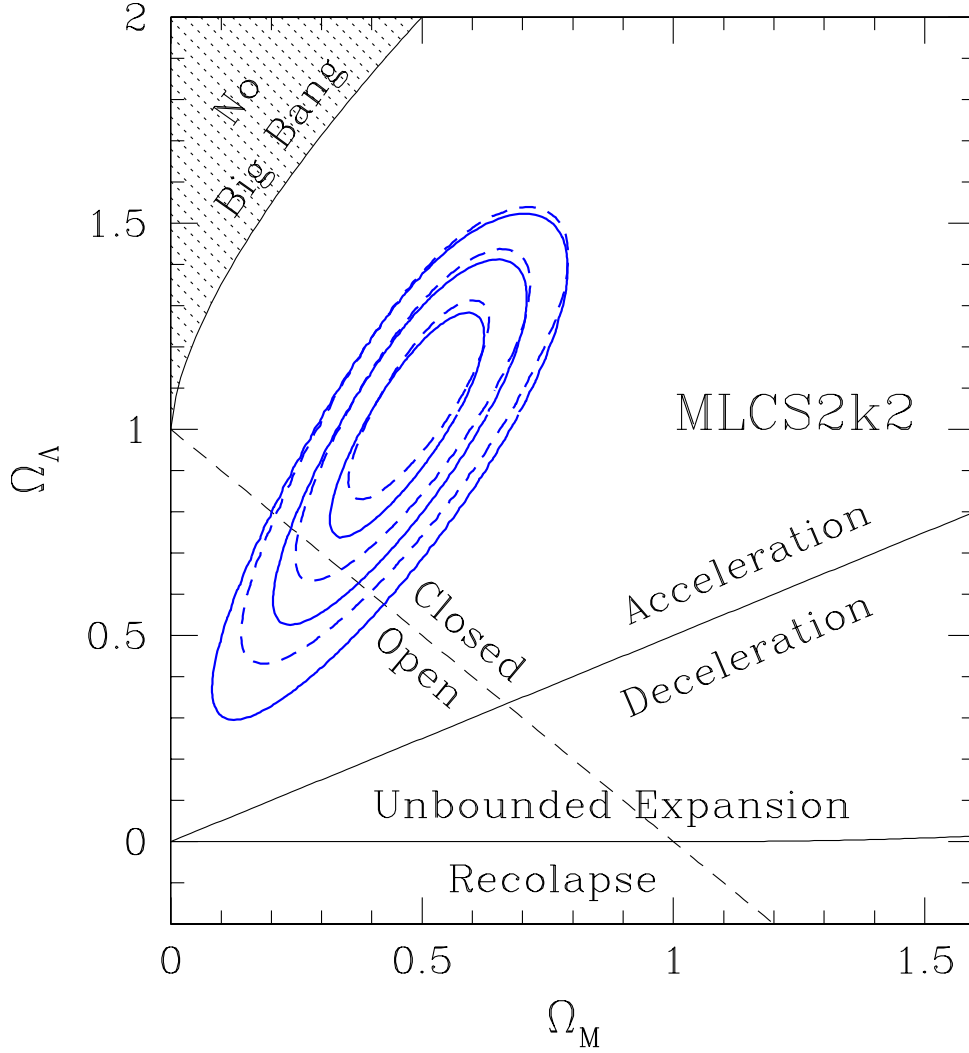


Fig. 21.— The dashed line shows the joint probability contours for the whole sample of “gold” and “silver” SNe of Riess et al. (2004), plus SNe 1999N, 1999Q, 1999S, and 1999U. The solid line shows only the “gold” SNe of Riess et al. (2004), plus the same four SNe of this campaign. In both cases, distances were calibrated using MLCS2k2.

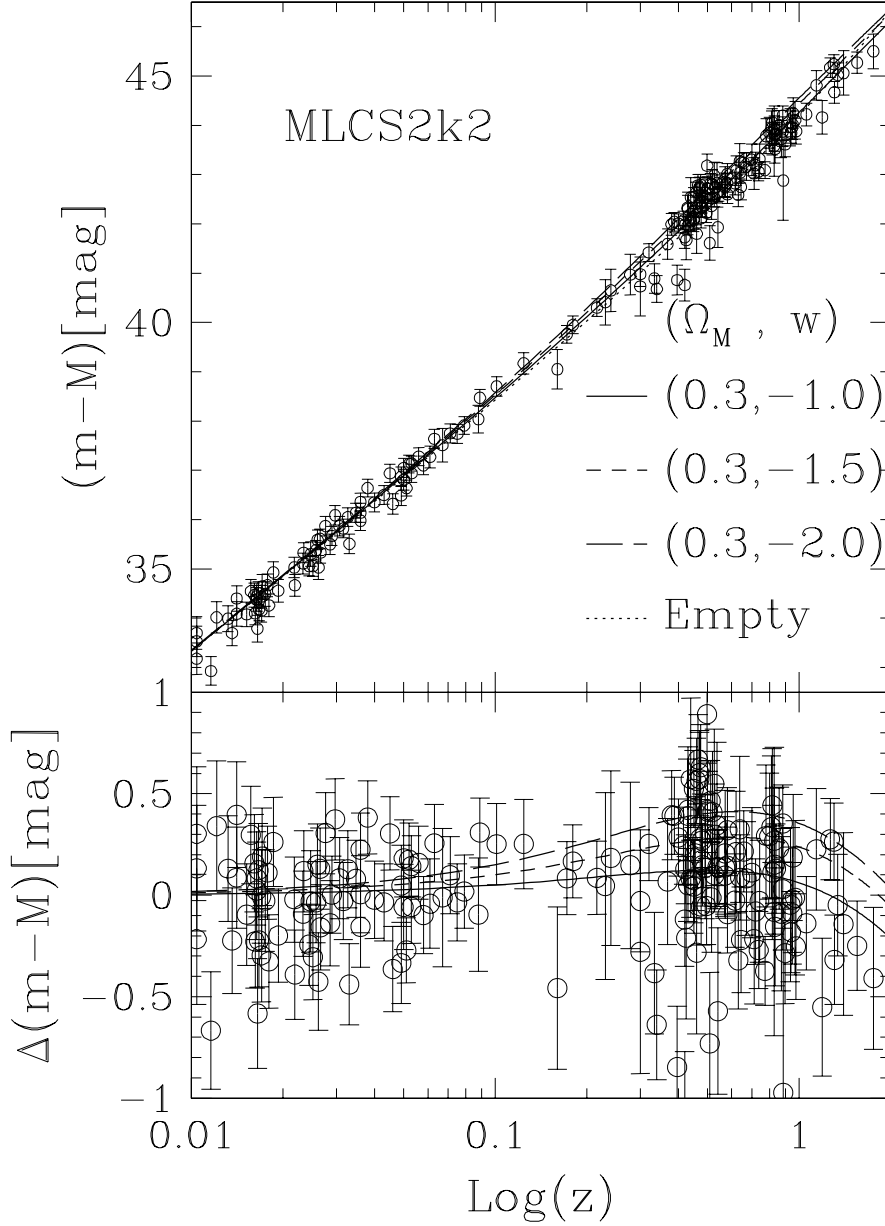


Fig. 22.— The Hubble diagram including the SNe presented in this study, using solid symbols, and those of Riess et al. (1998) and Tonry et al. (2003), using open symbols. Error bars correspond to 1σ . The upper panel shows the standard diagram, including the curves corresponding to the luminosity distances for universes with various parameters, as given in the legend. The lower panel shows the differential Hubble diagram, where the ordinate corresponds to the difference between the distance moduli observed (for SNe) and computed (for models) with the empty universe. The legend for line types is the same as in the upper panel.

Table 1. Observations of the Early 1999 Campaign

SN name	RA (2000.0)	Dec (2000.0)	Discovery ^a	$E(B-V)$ (mag)	N_{obs} ^b	HST
SN 1999M	10 05 46.60	−07 27 31.3	192.4	0.025	29	no
SN 1999N	10 04 27.93	−07 35 51.1	192.4	0.028	24	no
SN 1999Q	08 00 45.31	+05 31 27.4	193.2	0.021	83	yes
SN 1999S	09 28 08.08	−04 58 37.6	193.3	0.035	53	no
SN 1999U	09 26 42.96	−05 37 57.8	193.2	0.038	98	yes

^aMean Julian Date minus 2451000 days.

^bNumber of individual images taken. Many were later combined.

Table 2. Spectroscopy of the Selected Type Ia Supernovae

Name	Redshift ^a	Redshift Method	Exp. (s) ^b	Date ^c	Phase ^d		
					Sp. ^e	PRES ^f	MLCS2k2 ^g
1999M	0.493(1)	[O II] λ 3727 in host	4800	198.0	3	−1.3	...
1999N	0.537(5)	SN features	3000	198.0	3	3.8	3.6
1999Q	0.459(8)	SN features	24100	198.5	3	6.1	4.2
1999S	0.474(1)	[O II] λ 3727 in host	7200	197.0	−7	−7.9	−8.5
1999U	0.511(1)	[O II] λ 3727 in host	11400	197.5	−7	−6.2	−5.1

^aUncertainty in the last digit given in parentheses.

^bTotal exposure time in seconds.

^cMean Julian Date of exposures minus 2451000 days.

^dPhase in rest-frame days after B maximum.

^ePhase from spectroscopic match. Uncertainty estimated to be 4 days.

^fPhase implied by PRES light-curve fitting (see §4). Uncertainty estimated to be 2 days.

^gPhase implied by MLCS2k2 light-curve fitting (see §4). Uncertainty estimated to be 2 days.

Table 3. Photometric Sequence Near SN 1999M

ID	R	$R - I$
1	14.808 ± 0.003	0.372 ± 0.004
2	16.360 ± 0.003	1.132 ± 0.004
3	18.078 ± 0.007	0.916 ± 0.009
4	18.661 ± 0.017	0.483 ± 0.020
5	18.169 ± 0.006	0.802 ± 0.009
6	18.285 ± 0.010	0.437 ± 0.011
7	17.799 ± 0.003	0.517 ± 0.004
8	19.152 ± 0.014	0.428 ± 0.039
9	17.625 ± 0.003	1.457 ± 0.005
10	16.876 ± 0.004	0.564 ± 0.007
11	18.734 ± 0.004	0.952 ± 0.012
12	19.912 ± 0.006	0.765 ± 0.020
13	20.211 ± 0.030	1.127 ± 0.035
14	18.699 ± 0.007	0.894 ± 0.008
15	19.276 ± 0.010	1.102 ± 0.011
16	18.476 ± 0.011	0.766 ± 0.012
17	17.571 ± 0.007	1.183 ± 0.008
18	19.260 ± 0.020	0.412 ± 0.024
19	18.743 ± 0.004	0.362 ± 0.012
20	18.182 ± 0.007	0.985 ± 0.008
21	20.257 ± 0.007	0.749 ± 0.013
22	20.378 ± 0.015	0.678 ± 0.043

Table 4. Photometric Sequence Near SN 1999N

ID	R	$R - I$
1	17.505 ± 0.01	0.401 ± 0.012
2	17.73 ± 0.004	0.871 ± 0.007
3	17.388 ± 0.004	0.798 ± 0.007
4	16.245 ± 0.004	0.479 ± 0.007
5	17.377 ± 0.004	0.582 ± 0.007
6	17.571 ± 0.004	0.355 ± 0.008
7	17.956 ± 0.005	0.408 ± 0.008
8	17.106 ± 0.005	0.461 ± 0.007
9	18.396 ± 0.006	0.496 ± 0.01
10	16.268 ± 0.009	0.345 ± 0.01
11	16.138 ± 0.004	0.368 ± 0.006
12	17.914 ± 0.01	0.46 ± 0.012
13	18.618 ± 0.004	1.632 ± 0.007
14	17.434 ± 0.004	1.319 ± 0.007
15	18.08 ± 0.007	0.878 ± 0.009
16	18.836 ± 0.011	0.504 ± 0.013
17	17.794 ± 0.005	0.381 ± 0.008
18	16.954 ± 0.004	0.341 ± 0.007
19	14.997 ± 0.004	0.396 ± 0.006
20	18.898 ± 0.011	0.289 ± 0.015
21	18.513 ± 0.004	0.931 ± 0.008

Table 5. Photometric Sequence Near SN 1999Q

ID	R	$R - I$
1	18.947 ± 0.008	1.003 ± 0.011
2	19.983 ± 0.013	0.887 ± 0.020
3	20.105 ± 0.014	0.756 ± 0.020
4	18.925 ± 0.007	0.737 ± 0.011
5	18.933 ± 0.008	1.437 ± 0.021
6	19.016 ± 0.008	1.380 ± 0.011
7	19.186 ± 0.008	0.987 ± 0.012
8	19.889 ± 0.013	0.337 ± 0.023
9	21.471 ± 0.042	0.664 ± 0.065
10	19.753 ± 0.011	0.889 ± 0.017
11	21.210 ± 0.029	0.300 ± 0.063
12	19.875 ± 0.012	0.832 ± 0.018
13	18.471 ± 0.007	0.956 ± 0.010
14	18.218 ± 0.008	0.316 ± 0.014
15	21.174 ± 0.031	1.354 ± 0.037
16	20.792 ± 0.022	1.142 ± 0.031
17	15.355 ± 0.007	0.338 ± 0.010
18	17.216 ± 0.007	1.449 ± 0.010
19	19.867 ± 0.010	1.348 ± 0.014
20	21.313 ± 0.032	1.274 ± 0.042
21	19.639 ± 0.011	1.375 ± 0.014
22	21.198 ± 0.029	0.378 ± 0.069
23	21.699 ± 0.044	1.410 ± 0.057
24	17.103 ± 0.008	0.348 ± 0.011
25	20.769 ± 0.023	1.433 ± 0.028
26	20.897 ± 0.024	0.562 ± 0.040
27	21.069 ± 0.025	0.600 ± 0.047
28	15.345 ± 0.007	0.450 ± 0.010
29	20.812 ± 0.022	1.486 ± 0.027
30	22.011 ± 0.057	1.343 ± 0.068

Table 5—Continued

ID	R	$R - I$
31	18.395 ± 0.007	0.700 ± 0.012
32	19.860 ± 0.012	1.044 ± 0.017
33	21.143 ± 0.042	0.973 ± 0.065
34	18.571 ± 0.008	1.387 ± 0.011
35	21.478 ± 0.037	1.060 ± 0.051
36	19.707 ± 0.011	0.978 ± 0.015
37	18.523 ± 0.008	0.342 ± 0.011
38	18.814 ± 0.007	0.317 ± 0.011
39	17.147 ± 0.007	0.464 ± 0.010

Table 6. Photometric Sequence Near SN 1999S

ID	R	$R - I$
1	20.469 ± 0.031	0.527 ± 0.025
2	20.280 ± 0.018	1.502 ± 0.015
3	20.757 ± 0.027	1.397 ± 0.024
4	19.973 ± 0.016	0.949 ± 0.014
5	16.605 ± 0.002	0.949 ± 0.002
6	19.440 ± 0.014	0.485 ± 0.011
7	20.148 ± 0.017	1.180 ± 0.015
8	19.202 ± 0.012	0.462 ± 0.010
9	15.178 ± 0.001	0.361 ± 0.001
10	19.809 ± 0.012	1.479 ± 0.011
11	19.587 ± 0.014	0.790 ± 0.011
12	15.855 ± 0.001	0.402 ± 0.001
13	17.087 ± 0.004	0.320 ± 0.003
14	16.212 ± 0.002	0.331 ± 0.001
15	19.475 ± 0.016	0.370 ± 0.012
16	18.980 ± 0.009	0.965 ± 0.007
17	16.439 ± 0.002	0.453 ± 0.001

Table 7. Photometric Sequence Near SN 1999U

ID	R	$R - I$
1	20.771 ± 0.038	1.058 ± 0.030
2	18.338 ± 0.004	1.496 ± 0.004
3	19.614 ± 0.023	0.347 ± 0.017
4	21.069 ± 0.036	1.787 ± 0.032
5	19.997 ± 0.032	0.280 ± 0.024
6	19.716 ± 0.011	1.673 ± 0.010
7	18.893 ± 0.006	1.578 ± 0.006
8	15.808 ± 0.001	0.399 ± 0.001
9	20.916 ± 0.036	1.341 ± 0.030
10	18.763 ± 0.009	1.159 ± 0.008
11	19.397 ± 0.011	0.890 ± 0.009
12	19.376 ± 0.018	0.345 ± 0.013
13	21.127 ± 0.064	0.572 ± 0.049
14	19.830 ± 0.013	1.611 ± 0.011
15	19.156 ± 0.012	0.778 ± 0.009
16	21.241 ± 0.046	1.388 ± 0.038
17	21.068 ± 0.052	0.909 ± 0.042
18	19.592 ± 0.025	0.373 ± 0.020
19	21.564 ± 0.062	1.253 ± 0.051
20	21.057 ± 0.042	1.280 ± 0.034
21	20.042 ± 0.017	1.286 ± 0.014
22	20.927 ± 0.044	1.056 ± 0.036
23	21.405 ± 0.049	1.540 ± 0.041
24	21.816 ± 0.084	1.259 ± 0.070
25	20.807 ± 0.061	0.314 ± 0.046
26	20.616 ± 0.045	0.504 ± 0.035
27	19.992 ± 0.033	0.504 ± 0.026
28	17.728 ± 0.004	1.294 ± 0.003
29	20.529 ± 0.022	1.611 ± 0.020
30	18.014 ± 0.005	0.516 ± 0.004
31	19.972 ± 0.031	0.248 ± 0.023

Table 7—Continued

ID	R	$R - I$
32	21.121 ± 0.085	0.293 ± 0.063
33	17.912 ± 0.005	0.958 ± 0.004
34	18.811 ± 0.012	1.044 ± 0.010

Table 8. Template Images

SN name	Passband	Telescope/Instrument	Exposure ^a	UT Date	Seeing ^b
1999M	R_c	CTIO 4.0m/BTC	900	1997/03/09	0.98
	I_c	VLT-1/FORS-1	1800	2000/02/05	0.86
1999N	R_c	CTIO 4.0m/BTC	900	1997/03/09	1.00
	I_c	VLT-1/FORS-1	1800	2000/02/07	0.84
1999Q	$F650W$	HST/WFPC2	1600	2000/03/14	0.15
	$F650W$	HST/WFPC2 (v.2) ^c	11200	1999/02/07-2000/03/14	0.55
	$F814W$	HST/WFPC2	2400	2000/03/14	0.15
	$F814W$	HST/WFPC2 (v.2) ^c	16800	1999/02/07-2000/03/14	0.55
1999S	R_c	UH 2.2m/CCD Camera	1080	1999/12/18	0.83
	R_c	ESO 2.2m/WFI	900	2001/04/20	0.90
	R_c	CTIO 4.0m/Mosaic II	720	2001/04/13	0.97
	I_c	CTIO 4.0m/BTC	780	1998/01/24	0.95
1999U	$F650W$	HST/WFPC2	1600	2000/03/14	0.15
	$F650W$	HST/WFPC2 (v.2) ^c	11200	1999/02/07-2000/03/14	0.55
	R_c	Baade/LDSS2	360	2002/01/18	0.90
	I_c	CTIO 4.0m/BTC	780	1998/01/23	1.12
	$F814W$	HST/WFPC2	2400	2000/03/14	0.15
	$F814W$	HST/WFPC2 (v.2) ^c	16800	1999/02/07-2000/03/14	0.55

^aTotal exposure time in seconds.

^bFWHM of PSF in arcseconds.

^cTemplate image version 2 built from all *HST* observations (see text).

Table 9. Photometry and K -corrections of SN 1999M

Date ^a	m_{obs} ^b	K_{ro} ^c	Exp. (s) ^d	Telescope	Filter
$K_{Passband \rightarrow B}$					
191.85	23.230 ± 0.050	-0.717 ± 0.008	450	CTIO 4.0m	R_c
196.81	23.125 ± 0.059	-0.710 ± 0.008	300	CTIO 4.0m	R_c
198.78	23.251 ± 0.090	-0.719 ± 0.009	2440	CTIO 1.5m	B45
225.98	24.178 ± 0.068	-0.719 ± 0.008	1800	UH 2.2m	R_c
$K_{Passband \rightarrow V}$					
198.79	22.100 ± 0.153	-0.843 ± 0.013	1840	CTIO 1.5m	V45
225.99	23.165 ± 0.105	-0.840 ± 0.008	3600	UH 2.2m	I_c

^aMJD – 2451000.

^bObserved-frame magnitudes.

^c K -correction computed with PRES light-curve fitting.

^dCumulative exposure time in seconds.

Table 10. Photometry and K-corrections of SN 1999N

Date ^a	m_{obs} ^b	K_{ro} ^c	K_{ro} ^d	Exp. (s) ^e	Telescope	Filter
		$K_{Passband \rightarrow B}$	$K_{Passband \rightarrow B}$			
191.85	23.150 ± 0.028	-0.674 ± 0.029	-0.690 ± 0.005	450	CTIO 4.0m	R_c
196.81	23.139 ± 0.046	-0.664 ± 0.029	-0.692 ± 0.013	300	CTIO 4.0m	R_c
198.81	23.268 ± 0.122	-0.678 ± 0.031	-0.686 ± 0.006	1200	CTIO 1.5m	B45
219.06	24.755 ± 0.068	-0.636 ± 0.029	-0.649 ± 0.013	300	Keck-2	R^f
225.01	25.006 ± 0.125	-0.633 ± 0.029	-0.665 ± 0.001	3000	UH 2.2m	R_c
		$K_{Passband \rightarrow V}$	$K_{Passband \rightarrow V}$			
207.86	23.458 ± 0.502	-0.830 ± 0.031	-0.853 ± 0.005	1080	CTIO 1.5m	V45
219.06	24.544 ± 0.265	-0.806 ± 0.020	-0.825 ± 0.009	300	Keck-2	I^f
225.01	24.272 ± 0.434	-0.781 ± 0.020	-0.825 ± 0.018	3600	UH 2.2m	I_c

^aMJD – 2451000.

^bObserved-frame magnitudes.

^cK-correction computed with PRES light-curve fitting.

^dK-correction computed with MLCS2k2 light-curve fitting.

^eCumulative exposure time in seconds.

^fKeck-2 passbands have non-standard transmission curves.

Table 11. Photometry and K-corrections of SN 1999Q

Date ^a	m_{obs} ^b	K_{ro} ^c	K_{ro} ^d	Exp. (s) ^e	Telescope	Filter
		$K_{Passband \rightarrow B}$	$K_{Passband \rightarrow B}$			
197.690	22.417 ± 0.017	-0.712 ± 0.008	-0.702 ± 0.001	2700	APO 3.5m	B45
198.630	22.479 ± 0.034	-0.713 ± 0.008	-0.702 ± 0.001	4520	CTIO 1.5m	B45
199.740	22.573 ± 0.018	-0.715 ± 0.008	-0.702 ± 0.001	2640	ESO 3.6m	B45
210.223	23.048 ± 0.037	-0.844 ± 0.040	-0.743 ± 0.026	1600	HST	F675W
216.219	23.405 ± 0.047	-0.891 ± 0.040	-0.819 ± 0.040	1600	HST	F675W
219.000	23.807 ± 0.040	-0.787 ± 0.010	-0.714 ± 0.001	500	Keck-2	R^f
219.610	23.806 ± 0.048	-0.733 ± 0.008	-0.710 ± 0.001	3600	APO 3.5m	B45
223.449	23.872 ± 0.066	-0.934 ± 0.040	-0.912 ± 0.013	1600	HST	F675W
227.760	24.160 ± 0.054	-0.807 ± 0.010	-0.717 ± 0.001	720	Keck-2	R^f
230.730	24.253 ± 0.089	-0.956 ± 0.040	-0.940 ± 0.005	1600	HST	F675W
237.430	24.569 ± 0.115	-0.955 ± 0.040	-0.930 ± 0.001	1600	HST	F675W
244.422	24.817 ± 0.146	-0.941 ± 0.040	-0.947 ± 0.005	1600	HST	F675W
		$K_{Passband \rightarrow V}$	$K_{Passband \rightarrow V}$			
192.690	22.279 ± 0.027	-0.857 ± 0.008	-0.863 ± 0.001	2340	CTIO 4.0m	I_c
199.670	22.290 ± 0.037	-0.836 ± 0.008	-0.838 ± 0.003	4320	ESO 3.6m	V45
210.289	22.668 ± 0.030	-0.771 ± 0.013	-0.791 ± 0.006	2400	HST	F814W
216.270	22.871 ± 0.032	-0.773 ± 0.013	-0.788 ± 0.008	2400	HST	F814W
219.010	23.010 ± 0.072	-0.853 ± 0.008	-0.825 ± 0.014	360	Keck-2	I^f
219.650	22.945 ± 0.080	-0.829 ± 0.008	-0.869 ± 0.004	1800	ESO 3.6m	I_c
223.473	23.149 ± 0.040	-0.779 ± 0.013	-0.804 ± 0.007	2400	HST	F814W
224.850	23.217 ± 0.090	-0.861 ± 0.008	-0.875 ± 0.003	2400	UH 2.2m	I_c
225.810	23.245 ± 0.110	-0.863 ± 0.008	-0.876 ± 0.003	2700	UH 2.2m	c
230.784	23.374 ± 0.048	-0.778 ± 0.013	-0.820 ± 0.007	2400	HST	F814W
237.445	23.675 ± 0.058	-0.769 ± 0.013	-0.843 ± 0.003	2400	HST	F814W
244.432	23.959 ± 0.071	-0.760 ± 0.013	-0.826 ± 0.007	2400	HST	F814W

^aMJD – 2451000.

^bObserved-frame magnitudes.

^cK-correction computed with PRES light-curve fitting.

^dK-correction computed with MLCS2k2 light-curve fitting.

^dCumulative exposure time in seconds.

^fKeck-2 passbands have non-standard transmission curves.

Table 12. Photometry and K-corrections of SN 1999S

Date ^a	m_{obs} ^b	K_{ro} ^c	K_{ro} ^d	Exp. (s) ^e	Telescope	Filter
		$K_{Passband \rightarrow B}$	$K_{Passband \rightarrow B}$			
198.700	22.563 ± 0.028	-0.718 ± 0.005	-0.715 ± 0.001	3608	CTIO 1.5m	B45
206.820	22.122 ± 0.016	-0.717 ± 0.005	-0.715 ± 0.001	3284	CTIO 1.5m	B45
219.040	22.281 ± 0.014	-0.716 ± 0.006	-0.721 ± 0.001	240	Keck-2	R^f
224.750	22.509 ± 0.028	-0.715 ± 0.005	-0.709 ± 0.003	2400	APO 3.5m	B45
225.880	22.650 ± 0.030	-0.730 ± 0.006	-0.728 ± 0.007	1800	UH 2.2m	R_c
		$K_{Passband \rightarrow V}$	$K_{Passband \rightarrow V}$			
192.770	23.421 ± 0.033	-0.855 ± 0.005	-0.878 ± 0.002	2340	CTIO 4.0m	I_c
206.820	22.326 ± 0.061	-0.849 ± 0.009	-0.865 ± 0.006	1800	CTIO 1.5m	V45
219.040	22.241 ± 0.010	-0.863 ± 0.020	-0.825 ± 0.009	450	Keck-2	I^f
225.910	22.428 ± 0.016	-0.852 ± 0.005	-0.866 ± 0.001	3600	UH 2.2m	I_c

^aMJD – 2451000.

^bObserved-frame magnitudes.

^cK-correction computed with PRES light-curve fitting.

^dK-correction computed with MLCS2k2 light-curve fitting.

^eCumulative exposure time in seconds.

^fKeck-2 passbands have non standard transmission curves.

Table 13. Photometry and K-corrections of SN 1999U

Date ^a	m_{obs} ^b	K_{ro} ^c	K_{ro} ^d	Exp. (s) ^e	Telescope	Filter
		$K_{Passband \rightarrow B}$	$K_{Passband \rightarrow B}$			
197.77	22.783 ± 0.035	-0.730 ± 0.020	-0.716 ± 0.005	1800	APO 3.5m	B45
198.73	22.736 ± 0.050	-0.728 ± 0.020	-0.714 ± 0.009	2990	CTIO 1.5m	B45
199.83	22.654 ± 0.027	-0.727 ± 0.020	-0.711 ± 0.009	1980	ESO 3.6m	B45
210.36	22.420 ± 0.023	-0.806 ± 0.019	-0.811 ± 0.004	1600	HST	F675W
216.41	22.650 ± 0.026	-0.818 ± 0.019	-0.804 ± 0.001	1600	HST	F675W
219.02	22.871 ± 0.021	-0.681 ± 0.008	-0.689 ± 0.005	486	Keck-1	R^f
223.53	23.050 ± 0.100	-0.830 ± 0.019	-0.808 ± 0.005	1600	HST	F675W
224.90	23.179 ± 0.053	-0.680 ± 0.008	-0.704 ± 0.001	1800	UH 2.2m	R_c
230.87	23.470 ± 0.044	-0.838 ± 0.019	-0.826 ± 0.009	1600	HST	F675W
237.51	23.970 ± 0.054	-0.840 ± 0.019	-0.839 ± 0.003	1600	HST	F675W
244.49	24.440 ± 0.074	-0.840 ± 0.019	-0.836 ± 0.003	1600	HST	F675W
		$K_{Passband \rightarrow V}$	$K_{Passband \rightarrow V}$			
192.73	23.038 ± 0.038	-0.885 ± 0.013	-0.909 ± 0.004	2340	CTIO 4.0m	I_c
199.80	22.535 ± 0.051	-0.857 ± 0.021	-0.876 ± 0.007	3600	ESO 3.6m	V45
210.38	22.320 ± 0.026	-0.824 ± 0.021	-0.788 ± 0.001	2400	HST	F814W
216.43	22.470 ± 0.027	-0.804 ± 0.021	-0.788 ± 0.001	2400	HST	F814W
219.02	22.702 ± 0.035	-0.852 ± 0.013	-0.845 ± 0.007	480	Keck-1	I^f
219.75	22.595 ± 0.055	-0.831 ± 0.021	-0.822 ± 0.007	2400	APO 3.5m	V45
223.55	22.660 ± 0.062	-0.771 ± 0.021	-0.788 ± 0.001	2400	HST	F814W
224.93	22.704 ± 0.074	-0.840 ± 0.013	-0.858 ± 0.008	3000	UH 2.2m	I_c
230.92	23.030 ± 0.033	-0.737 ± 0.021	-0.788 ± 0.001	2400	HST	F814W
237.52	23.380 ± 0.041	-0.713 ± 0.021	-0.788 ± 0.001	2400	HST	F814W
244.51	23.610 ± 0.047	-0.693 ± 0.021	-0.788 ± 0.001	2400	HST	F814W

^aMJD – 2451000.

^bObserved-frame magnitudes.

^cK-correction computed with PRES light-curve fitting.

^dK-correction computed with MLCS2k2 light-curve fitting.

^dCumulative exposure time in seconds.

^fKeck-2 passbands have non standard transmission curves.

Table 14. Parameters of the Light-Curve Fits (PRES method)

SN	z	$E(B - V)_{\text{Gal.}}$	μ (mag)	Δm_{15} (mag) ^a	$E(B - V)_{\text{Host}}$	t_{max}^B ^b
1999M	0.493	0.042	41.02 ± 0.81	0.83 ± 0.18	0.61 ± 0.20	199.8
1999N	0.537	0.050	43.11 ± 0.20	1.22 ± 0.15	0.00 ± 0.03	192.2
1999Q	0.459	0.021	42.63 ± 0.14	0.83 ± 0.02	0.05 ± 0.03	189.6
1999S	0.474	0.033	42.55 ± 0.20	0.87 ± 0.02	0.00 ± 0.03	210.0
1999U	0.511	0.039	42.48 ± 0.16	1.02 ± 0.04	0.06 ± 0.03	207.1

^aMagnitudes below rest-frame B maximum.

^b $\text{JD}_{\text{max}} - 2,451,000$ days.

Table 15. Parameters of the Light-Curve Fits (MLCS2k2 method)

SN	z	$E(B - V)_{\text{Gal.}}$	μ (mag)	$E(B - V)_{\text{Host}}$	t_{max}^B ^a
1999N	0.537	0.050	42.81 ± 0.41	0.18	192.4
1999Q	0.459	0.021	42.62 ± 0.21	0.19	192.3
1999S	0.474	0.033	42.77 ± 0.21	-0.07	209.6
1999U	0.511	0.039	42.80 ± 0.20	0.18	205.2

^a $\text{JD}_{\text{max}} - 2,451,000$ days.

Table 16. Fits to Λ CDM Cosmology

Method	Constraint	Ω_M^a	Ω_Λ^a	χ^2	N ^b
<u>All HZT SNe except this work</u>					
MLCS2k2	none	$0.68^{+0.18}_{-0.26}$	$1.20^{+0.34}_{-0.41}$	109	118
PRES	none	$0.27^{+0.17}_{-0.19}$	$0.88^{+0.29}_{-0.27}$	112	101
MLCS2k2	$\Omega_M + \Omega_\Lambda = 1$	$0.33^{+0.07}_{-0.05}$	$1 - \Omega_M$	107	118
PRES	$\Omega_M + \Omega_\Lambda = 1$	$0.20^{+0.05}_{-0.04}$	$1 - \Omega_M$	112	101
<u>All HZT SNe</u>					
MLCS2k2	none	$0.79^{+0.15}_{-0.18}$	$1.57^{+0.24}_{-0.32}$	118	122
PRES	none	$0.43^{+0.17}_{-0.19}$	$1.18^{+0.27}_{-0.28}$	133	106
MLCS2k2	$\Omega_M + \Omega_\Lambda = 1$	$0.29^{+0.06}_{-0.05}$	$1 - \Omega_M$	124	122
PRES	$\Omega_M + \Omega_\Lambda = 1$	$0.18^{+0.05}_{-0.04}$	$1 - \Omega_M$	132	106
<u>SNe of this work plus gold & silver of Riess et al. (2004)</u>					
MLCS2k2	none	$0.50^{+0.10}_{-0.10}$	$1.10^{+0.16}_{-0.17}$	219	187
MLCS2k2	$\Omega_M + \Omega_\Lambda = 1$	$0.29^{+0.04}_{-0.03}$	$1 - \Omega_M$	224	187
<u>SNe of this work plus gold of Riess et al. (2004)</u>					
MLCS2k2	none	$0.48^{+0.09}_{-0.12}$	$1.04^{+0.17}_{-0.19}$	184	158
MLCS2k2	$\Omega_M + \Omega_\Lambda = 1$	$0.30^{+0.04}_{-0.04}$	$1 - \Omega_M$	186	158

^a 1σ uncertainties

^bNumber of SNe for this sample and method.